CHEMISTRY
A EUROPEAN JOURNAL

FULL PAPER

DOI: 10.1002/chem.201203758

# Pseudo-Fivefold Diffraction Symmetries in Tetrahedral Packing

**Stephen Lee,* Ryan Henderson, Corey Kaminsky, Zachary Nelson, Jeffers Nguyen, Nick F. Settje, Joshua Teal Schmidt, and Ji Feng[a]**

**Abstract:** We review the way in which atomic tetrahedra composed of metallic elements pack naturally into fused icosahedra. Orthorhombic, hexagonal, and cubic intermetallic crystals based on this packing are all shown to be united in having pseudo-fivefold rotational diffraction symmetry. A unified geometric model involving the 600-cell is presented: the model accounts for the observed pseudo-fivefold symmetries among the different Bravais lattice types. The model accounts for vertex-, edge-, polygon-, and cell-centered fused-icosahedral clusters. Vertex-centered and edge-centered types correspond to the well-known pseudo-fivefold symmetries in $I_h$ and $D_{5h}$ quasicrystalline approximants. The concept of a tetrahedrally-packed reciprocal space cluster is introduced, the vectors between sites in this cluster corresponding to the principal diffraction peaks of fused-icosahedrally-packed crystals. This reciprocal-space cluster is a direct result of the pseudosymmetry and, just as the real-space clusters, can be rationalized by the 600-cell. The reciprocal space cluster provides insights for the Jones model of metal stability. For tetrahedrally-packed crystals, Jones zone faces prove to be pseudosymmetric with one another. Lower and upper electron per atom bounds calculated for this pseudosymmetry-based Jones model are shown to accord with the observed electron counts for a variety of Group 10–12 tetrahedrally-packed structures, among which are the four known Cu/Cd intermetallic compounds: $CdCu_2$, $Cd_3Cu_4$, $Cu_5Cd_8$, and $Cu_3Cd_{10}$. The rationale behind the Jones lower and upper bounds is reviewed. The crystal structure of $Zn_{11}Au_{15}Cd_{23}$, an example of a 1:1 MacKay cubic quasicrystalline approximant based solely on Groups 10–12 elements is presented. This compound crystallizes in $Im\bar{3}$ (space group no. 204) with $a = 13.842(2)$ Å. The structure was solved with $R_1 = 3.53\,\%$, $I > 2\sigma; = 5.33\,\%$, all data with 1282/0/38 data/restraints/parameters.

**Keywords:** diffraction · intermetallic phases · noble metals · quasicrystals · solid state structures

## Introduction

Tetrahedral packing in metal crystals is ubiquitous; it is also complex.[1–4] While tetrahedra combined with octahedra fill space in the well-known face-centered-cubic and hexagonal-closest-packed structures, tetrahedral packing leads to the Frank–Kasper phases,[5–8] structures such as the Laves phases,[9,10] $Al_6Mg_{11}Zn_{11}$,[11] and $Cd_3Cu_4$,[12–14] with unit cells extending from tens to hundreds or even thousands of atoms.[15–20]

Worse yet for their understanding, perfect regular tetrahedra do not fill space. While tetrahedra plus octahedra assemble into clusters of easily discerned octahedral or hexagonal symmetry, symmetries which naturally extend into the crystal symmetry as a whole, twenty tetrahedra come together to make a filled icosahedron, a cluster whose fivefold rotations bear little relation to crystal symmetries.

In this paper we will discuss the most regular of tetrahedral cluster packing, packing in which tetrahedra come together to make filled icosahedra. We will show how, in these cases, pure tetrahededral packing may not lead to true crystal symmetries, but in general leads to a variety of pseudo fivefold rotational symmetries. We will find that the bonds at the center of these tetrahedral clusters form the pseudo-fivefold rotation axes, rotation axes which can be shown to dominate the single crystal x-ray diffraction patterns.[8,12,21,22] We will see that tetrahedrally-packed icosahedral and decagonal quasicrystals are just two of four limiting cases.

We will further show the symmetries of the strongest diffraction peaks are not only controlled by the central bonds of the tetrahedral clusters, but that, viewed as vectors, the directions defined by these strongest diffraction peaks actually *are* the directions of the central bonds. We will find these strong diffraction peaks viewed as vectors form reciprocal space clusters of unusual shape and pseudosymmetry.

Examining these diffraction peaks, we can apply the Jones theory of intermetallic stability,[23–25] a quantum theory which connects strong diffraction to optimal numbers of valence electrons, and which, as we further discuss in this paper, can be beneficially related to tight-binding and extended Hückel theories.[26–28] We therefore relate tetrahedral packing to possible atomic stoichiometries and connect the

[a] Prof. S. Lee, Dr. R. Henderson, C. Kaminsky, Z. Nelson, J. Nguyen, N. F. Settje, Dr. J. T. Schmidt, Dr. J. Feng
Department of Chemistry and Chemical Biology
Cornell University, Ithaca, NY 14853-1301 (USA)
E-mail: sl137@cornell.edu

Supporting information for this article is available on the WWW under http://dx.doi.org/10.1002/chem.201203758.

tetrahedral cluster geometry to electronic structure and phase stability. The four known Cu–Cd compounds ($CdCu_2$,[29,30] $Cd_3Cu_4$,[12] $Cu_5Cd_8$,[31,32] and $Cu_3Cd_{10}$[33]) will be used to illustrate these relationships.

In this article, we consider four different limiting cases of tetrahedra packed into filled icosahedral clusters. In two of these, the clusters will be of respectively $I_h$ and $D_{5h}$ symmetry, known quasicrystal point groups.[34–38] In the other two cases, the clusters will prove to be of $T_d$ and $D_{3h}$ symmetry and will result in, respectively, cubic and hexagonal crystalline structures. The literature has found common ground for these structures as projections of six-[39–42] or eight-dimensional[43–47] Bravais lattices, curved topology,[21,48,49] and networks of disclinations.[50–52] The current work pares these mathematical approaches to their bare minimum, that is, to concepts which describe concrete 3D crystals: the 3D pseudosymmetries, the pseudo-equivalences of their 3D diffraction reflections, and the tetrahedral organization of both their 3D real and reciprocal space clusters.

## Results and Discussion

**Aufbau of tetrahedral clusters**: In the plane, six equilateral triangles pack perfectly around a single atom (Figure 1). The analogous 3D question of how many tetrahedra can be placed around a single atom is more difficult. As Figure 1 shows, one can place twenty tetrahedra around an atom, but the resultant cluster has deep crevasses, and is not suitable for the packing of atoms. To remove these crevasses, we must make the tetrahedra slightly irregular. If half of the six edges of the tetrahedra are 95% the length of the other half, the twenty slightly irregular tetrahedra coalesce into a single filled and perfect icosahedron (see Figure 1) with all crevasses between tetrahedra removed.

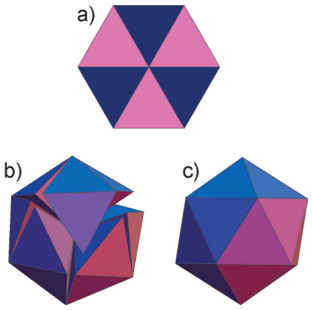


Figure 1. a) Six equilateral triangles joined together into a regular planar hexagon and either b) twenty face-sharing regular tetrahedra joined into an icosahedral shape with crevasses or c) twenty slightly-irregular tetrahedra fused into a regular icosahedron.

In exactly the same way, we can pose the question of the best way of placing tetrahedra around a pair of atoms. The answer, as is shown in Figure 2, is five, though once again the tetrahedra must be made slightly irregular. If we add tetrahedra at the two ends of this ring of tetrahedra, we end up with the cluster shown in Figure 3. Each of the central atoms now has twenty tetrahedra around it, each of these twenty tetrahedra form imperfect icosahedra. The overall cluster has nineteen atoms to it. As Figure 3 shows, this cluster can be viewed as the fusing of two filled icosahedra. The cluster is composed of thirty-five tetrahedra, as the central five tetrahedra are part of both of the filled icosahedra. The cluster has $D_{5h}$ symmetry. As this cluster was built up from a pair of atoms lying along an edge of a tetrahedron, we refer to it as the edge-centered-cluster.

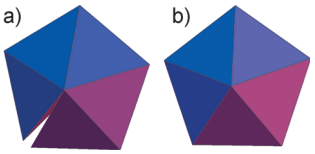


Figure 2. a) Five face-sharing regular tetrahedra joined into a fivefold ring with crevasses or b) five slightly-irregular tetrahedra fused into a $D_{5h}$ face-sharing ring of tetrahedra.

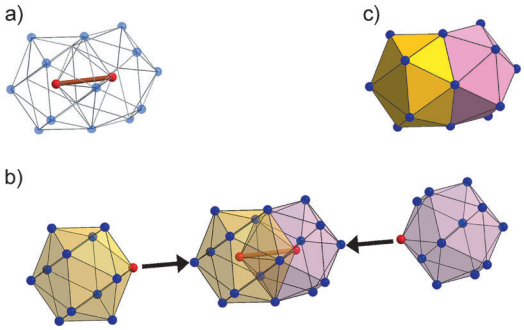


Figure 3. A pair of filled icosahedra fused into a single cluster, the edge-centered tetrahedral cluster. Single vertices from each icosahedron, indicated in red, come together to form an edge, shown in brown in the upper left inset. The cluster is of $D_{5h}$ point group symmetry. The shared volume shown in the center of panel b) is the same fused ring of tetrahedra shown (from another perspective) in Figure 2b. The full cluster shown here consists of 35 face-sharing tetrahedra.

In exactly the same way, we can ask the question of placing tetrahedra around a central equilateral triangle of atoms as well as around a central tetrahedron itself. These two clusters are shown in Figures 4 and 5, respectively. They consist of 47 and 57 tetrahedra derived from, respectively, three and four fused icosahedra. The two clusters are of, respectively, $D_{3h}$ and $T_d$ symmetry. They are referred to in this paper, respectively, as the polygon-centered cluster and the cell-centered cluster. The term cell used here follows the mathematics literature and is used in this case to describe the central tetrahedron of the cluster, the term tetrahedrally-centered cluster being something of a mental conundrum in the description of a tetrahedrally based structure. Polygon-centered refers to the equilateral triangle, a polygon, at the cluster center.

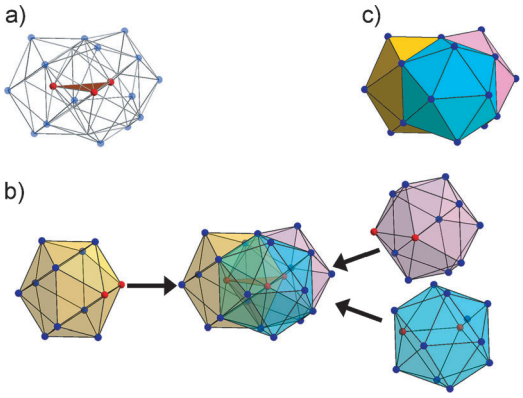


Figure 4. Three filled icosahedra fused into a single cluster, the polygon-centered tetrahedral cluster. Edges from each icosahedron, indicated by pairs of red-colored vertices, come together to form an equilateral triangle, a polygon, shown in brown in the upper left inset. The cluster is of $D_{3h}$ point group symmetry and consists of 47 face-sharing tetrahedra.

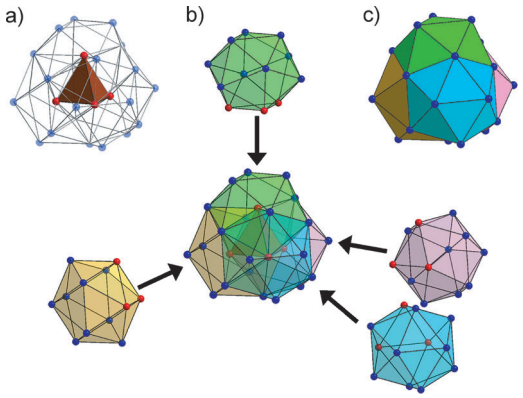


Figure 5. Four filled icosahedra fused into a single cluster, the cell-centered tetrahedral cluster. Faces from each icosahedron, indicated by triangles of red-colored vertices, come together to form a tetrahedron, a cell, shown in brown in the upper left inset. The cluster is of $T_d$ point group symmetry and consists of 57 face-sharing tetrahedra.

**A unified view for tetrahedral clusters**: In the previous section we have examined four different tetrahedral clusters, clusters whose centers are a vertex, an edge, a triangular polygon, or a tetrahedral cell, respectively. All central atoms in all the four clusters lie in the center of icosahedra. We now show an exact connection between these clusters, a connection best understood by the following analogy. In Figure 6 we show three different planar arrangements of atoms: the first has a single pentagon with an atom at its center, the second has two such filled pentagons around a central edge, while the third has three filled pentagons built around a common polygon. These three fused pentagonal arrangements can be viewed as 2D analogs of the four tetrahedral clusters discussed in the previous section.

The crux to the analogy is that while as 2D figures, the vertex-, edge-, and polygon-centered arrangements of Figure 6 are all distinct from one another, as the lower panel of this Figure shows, they can also be viewed as orthographic hemispheric projections of the same three-dimensional cluster (an orthographic hemispheric projection is a standard orthographic projection where one explicitly limits oneself to just one hemisphere). This 3D cluster is the icosahedron, one of the most symmetric 3D Platonic solids.

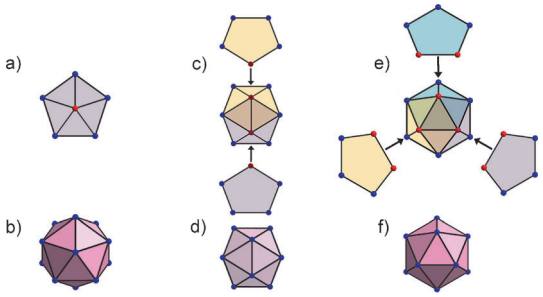


Figure 6. 2D a) single filled-, c) two edge-centered fused-, and e) three polygon-centered fused-pentagons forming the projected shapes of a 3D icosahedron orthographically projected down, respectively, a b) vertex, d) edge, and f) face. While there is a one-to-one correspondence between vertices in the center portion of c) and d) as well as the center portion of e) and f), one would have to restrict oneself to just a single hemisphere of the orthographic projection, b), to exactly coincide with the single-filled pentagon in a).

In exactly the same manner, the vertex-, edge-, polygon-, and cell-centered tetrahedral clusters can be shown to be orthographic hemispheric projections of the same 4D structure, a 4D Platonic solid.[8,21,22,45,46,53] In making orthographic hemispheric projections, one needs to decide whether atoms at the equator itself should be included in the projection. As we discuss in specific detail in the Appendix, in this paper, 4D to 3D orthographic hemispheric projections do *not* include equatorial vertices. There are six 4D Platonic solids in total. Our interest is with one of the most symmetric 4D Platonic solids, the 600-cell.[54] The 600-cell contains 600 perfect tetrahedra and 120 vertices, all equidistant from the same 4D center. Each of these 120 vertices lies in the center of a perfect icosahedron. With twelve vertices to each icosahedron, the 600-cell contains 720 edges ($720=(120\times12)/2$). Every vertex, edge, face, tetrahedra, and icosahdedra are the same as all other vertices, edges, faces, tetrahedra, and icosahedra. The 600-cell is therefore Platonic.

In Figure 7 we show four 3D views of the 600-cell (see Supporting Information for the explicit 600-cell projection matrices). As this Figure shows, the central portion of the four views corresponds to the four different tetrahedral clusters discussed in the previous section. As this Figure also shows, however, these four tetrahedral clusters are surrounded by additional atoms. These additional atoms cap the triangular faces, thus generating further tetrahedra. For vertex-centered clusters it is traditional to include among the additional atoms those which cap vertices as well as faces. The vertex- edge-, polygon-, and cell-centered projections have, respectively, 45, 44, 50, and 54 atoms. Of the four cluster types, the vertex- and cell-centered clusters are best known. The former is termed the Bergman cluster while the latter is best known in γ-brass, $Cu_5Zn_8$.[11,22,32,55,56]

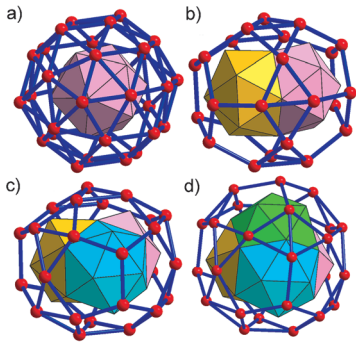


Figure 7. a) Vertex-, b) edge-, c) polygon-, and d) cell-centered hemispheric projection of the 4D Platonic solid, the 600-cell. The figures divide the projected 600-cell into inner- and outer-shells shown, respectively, as polyhedra and ball-and-stick figures. Inner shell colors refer to colors used in Figures 3–6. a) is the Bergman cluster. d) is found in γ-brass.

We will call the central portion of the vertex-, edge-, polygon-, and cell-centered projections, the single filled, pair of, trio of, and quarto of fused icosahedra, respectively, the inner shells of the clusters. The atoms capping the triangular faces of this inner shell will be termed the outer shell. For example, in the γ-brass structure it is traditional to focus on just the inner shell while for the Bergman cluster inner and outer shells are often viewed together. It should be noted that the vertex-, edge-, polygon-, and cell-centered projections are the only four 4D to 3D projections which correspond to isolated special points of higher symmetry. In a 3D globe to a 2D map projection, specifying the center of the projection, typically in this case a pole, completely specifies the projection itself. The same holds in the 4D to 3D projection. The symmetry of the "pole" taken in the 4D 600-cell to 3D projection therefore determines the symmetry of the projected 3D object. As the 600-cell is a 4D Platonic solid, there are only four high symmetry special points: they are, respectively, at the center of a vertex, an edge, a face or a cell, that is, they are the four projections shown in Figure 7.

While the 600-cell consists of 120 vertices, the four projections contain less than half the original 120 atoms. This reduction is a consequence of the 4D to 3D hemispheric projection. We can understand this reduction by the following analogy. When projecting a 3D sphere, the globe, onto a two-dimensional filled circle, a map, we project only half the sphere at a time. Simple projected maps of the Earth typically show just half the surface of the globe, typically either the Northern or Southern hemispheres. In our case, 3D hemispheric projections of it show just half of the 4D 600-cell, roughly 60 of the 120 vertices.

There is a further complication caused by the projection. It is in the region near the equator. In 3D, the equator is defined as the 2D circle which is projected the farthest away from the central pole. Euclidean features near the equator of a global map are always highly distorted. In 4D, the equator is the 3D sphere which projects furthest away from the pole.

Just as in the globe-to-map projection, geometrical features near the 4D equator are highly distorted upon projection into 3D space. Tetrahedra near the equator are unreasonable in shape (they are considerably flattened). Such flattened tetrahedra cannot be found in real 3D crystals and are therefore not included in our projected images. We therefore peel away these outermost tetrahedra from our hemispheric projected images; projected clusters therefore range from 44 to 54 atoms in size.

The edges of the 600-cell prove to be of significant chemical relevance. They can be the metal–metal bonds. But they serve other functions. First recall that the 600-cell is Platonic. In the original 600-cell the 720 edges are all symmetrically equivalent to one another. These 720 edges prove to define 720 fivefold rotations, all of which belong to the same class of the 600-cell point group. Relevant to us, these 720 4D edges all project into 3D incipient pseudo-fivefold rotational axes.

In the vertex-, edge-, polygon-, and cell-centered tetrahedral clusters there are 204, 193, 234, and 256 bonds, respectively. All of these edges retain, to some extent, symmetry aspects of the original 600-cell. But certain edges retain the symmetries to a much greater degree. An analogy to 2D projections of the 3D icosahedron helps illustrate this point. In an icosahedron, the triangular faces of the icosahedron are equilateral triangles. In Figure 6 we showed three different projected views of this icosahedron. As this Figure shows, those triangular faces closest to the center of the projection, retain to the greatest degree their threefold symmetry: they look most like equilateral triangles.

In a similar manner, those edges which lie closest to the center of the 3D tetrahedral-cluster projections retain the fivefold rotational symmetry of the original 4D 600-cell. We show this in Figure 8.

In this Figure we show the diffraction image along the most central edge for, respectively, the vertex-, edge-, polygon- and cell-centered projected 600-cell. As this Figure shows, there is discernible pseudo-fivefold diffractions along each of these edges. We further show in Figure 9 the diffraction image corresponding to the second-most central edge of the edge-centered cluster. For this cluster, this less central edge shows as well, albeit less markedly, pseudo-fivefold rotational symmetry. To generate the diffraction images for Figures 8 and 9, Dirac delta functions were placed at the atomic or polyhedral coordinates ($\delta(r-R_i)$), where $r$ is the position $(x,y,z)$ and $R$ is the $i$th atomic coordinate). In the case of the polyhedra, all Dirac delta functions were of unit volume and in the case of actual atomic clusters the volumes were weighted by the atomic number, $w_i$. The positions of the polyhedra were chosen to mimic intermetallic interatomic distances. The Fourier Transform was taken over the sum of the Dirac functions $\phi(k) = e^{-2\pi ik\cdot r} \Sigma w_i \delta(r-R_i)dr$.

Only the most central cluster edges correspond to pseudo-fivefold rotation axes, but less central cluster edges are also significant. Once we turn to real tetrahedral crystal structures, we will find the directions of the central edges point in the same direction as the principal diffraction

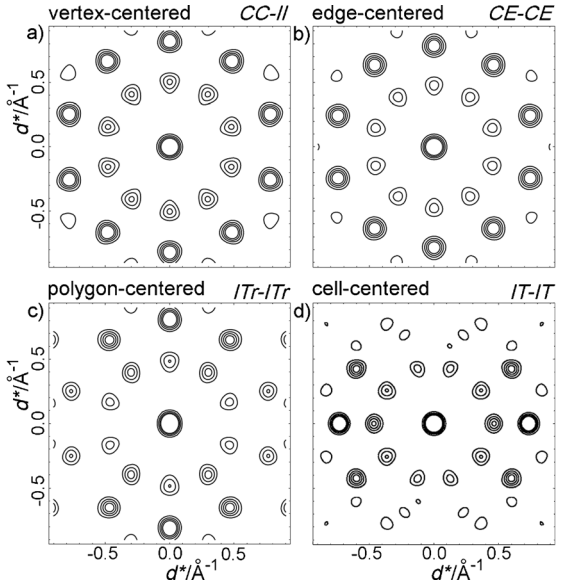


Figure 8. Diffraction pattern of a single a) 45-atom vertex-, b) 44-atom edge-, c) 50-atom polygon-, and d) 54-atom cell-centered cluster shown down an *CC–II*, *CE–CE*, *ITr–ITr*, and *IT–IT* cluster edge, respectively. Pseudo-fivefold rotational symmetries are seen in each of these diffraction patterns as 10-fold pseudosymmetric rosettes. Central cluster edges were chosen with average distances of 2.2 Å, corresponding to a value near the $d_{hkl}$ spacings in actual metal crystal structures, see Tables 1–5 and 7–11.

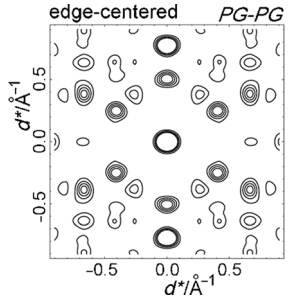


Figure 9. Diffraction pattern of a single 44-atom edge-centered cluster shown down its *PG–PG* cluster edge. Pseudo-fivefold symmetry is only somewhat recognizable. Interestingly, this diffraction pattern resembles the diffraction pattern of edge-centered cluster structures, shown in Figure 12, lower right, and 22, lower right, where pseudosymmetry is more obviously present.

peaks. Furthermore the *d*-spacing of these strongest diffraction peaks are roughly the same as the average bond lengths.

In general, the edges which are shared by more than one of the inner-shell fused icosahedra will be found to lead to the strongest diffraction. But significant intensity diffraction peaks will be derived from all inner shell edges. We show this hierarchy of edges for each of the four cluster types in Figure 10 going from central edges which display pseudo-fivefold diffraction symmetry (second column in the figure), to shared inner-shell edges which correspond to strongly diffracting directions (third column), to the remaining inner-shell edges which correspond to less strong, but still significant, diffraction peaks (fourth column).

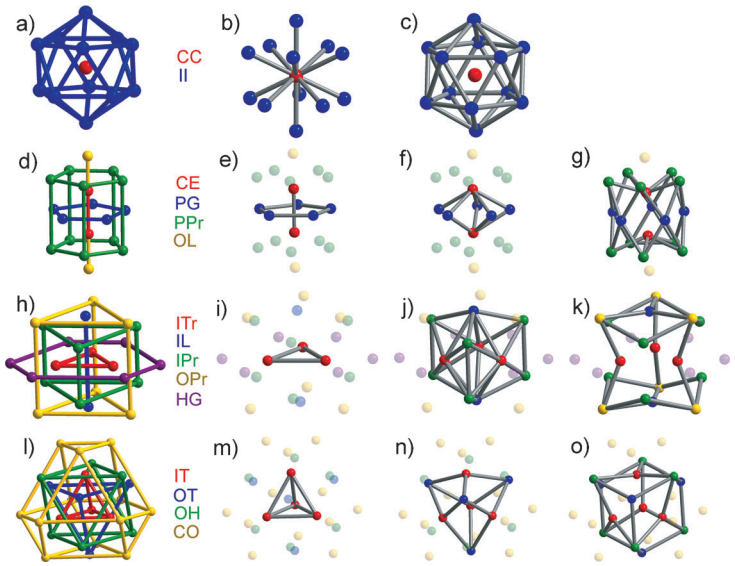


Figure 10. Site labeling scheme as well as representative edges for the inner shells of the different types of centered tetrahedral packing. First through fourth rows are for, respectively, vertex-, edge-, polygon-, and cell-centered clusters. First column: color-coded illustrations of the site labeling scheme (full site names given in text); second column: edges which correspond to pseudo-fivefold rotational axes; third column: together with the second column edges, the edges which correspond to the strongest diffraction peaks (see Section on cluster edges and diffraction and in particular Figure 24); and fourth column: the remaining edges whose corresponding diffraction peaks have significant, but not the strongest, intensities.

In describing these edges, it is useful to introduce a uniform nomenclature. In Figure 10, we can see that the cell-centered inner shell has four symmetry inequivalent sites. These sites are traditionally termed *I*nner *T*etrahedron (*IT*), *O*uter *T*etrahedron (*OT*), *O*cta*h*edron (*OH*), and *C*uboo*c*tahedron (*CO*). Of these four sites, only the *IT*, *OT*, and *OH* sites are shared by more than one of the inner-shell fused icosahedra. Those edges between *IT*, *OT*, and *OH* sites will prove to be the most strongly connected to the most intense diffracting reflections. And among this set of sites, the edges which correspond to the most discernable pseudo-fivefold symmetry are the most centrally located, the six *IT–IT* edges.

We can specify analogous nomenclatures for the vertex-, edge-, and polygon-centered clusters. The vertex-centered inner shell has two central symmetry inequivalent sites, the *C*luster *C*enter (*CC*) and the *I*nner *I*cosahedron (*II*) sites. For the edge-centered inner shell there are four symmetry inequivalent sites: *C*entral *E*dge (*CE*), *P*entagon (*PG*), *P*entagonal *Pr*ism (*PPr*), and *O*uter *L*ine (*OL*). Finally for the polygon-centered cluster, the central symmetry inequivalent sites are *I*nner *L*ine (*IL*), *I*nner *Tr*iangle (*ITr*), *I*nner *Pr*ism (*IPr*), *O*uter *Pr*ism (*OPr*), and *H*exagon (*HG*).

In the case of the vertex-centered cluster, the cluster is so symmetric that the entire projected 600-cell has only four symmetry inequivalent sites. Besides the *CC* and *II* sites, the cluster outer shell contains just two more site types, *OI*, the *O*uter *I*cosahedron and *DH*, the *D*odeca*h*edron. Less useful

but still sometimes in need of consideration are the outer shell sites in the remaining clusters. For edge-centered clusters we have the *O*uter *P*entagon (*OPg*), *El*ongated *P*entagonal *p*rism, (*ElPp*) and *Fl*attened *P*entagonal *p*rism (*FlPp*). For polygon-centered clusters the outer shell has four symmetry inequivalent sites: *H*exagonal *Pr*ism (*HgPr*), *El*ongated *Pr*ism (*ElPr*), *Fl*attened *Pr*ism (*FlPr*), and *O*uter *Tr*iangle (*OTr*). Finally for the cell-centered cluster the three sites are geometrically the *Ex*ternal *T*etrahedron (*ExT*), the *L*esser *T*runcated *t*etrahedron (*LsTt*), and the *Gr*eater *T*runcated *t*etrahedron (*GrTt*).

In considering atoms which lie on the central molecular axis, we distinguish those central atoms which are bonded to symmetry equivalent atoms versus those central atoms which are not bonded to symmetry equivalent atoms. We term these two cases, respectively, edge and line sites, as in versus *CE* for *C*entral *E*dge *CL* for *C*entral *L*ine. Where two letter designations are used for simple polyhedra and polygons, the second letters of the designation are, respectively, *H* for *h*edron and *G* for *g*on. It should be noted that the *HG* label has been applied to a hexagon of $D_{3h}$ rather than $D_{6h}$ symmetry. In the case of the outer shell of the cell-centered cluster the terms lesser and greater truncated tetrahedron refer to the degree of truncation present in the specified cluser. Finally where the type of prism is not specified, it is assumed to be a triangular prism.

**Crystalline examples of the four types of tetrahedral clusters**: Our interest is in finding crystals which preserve as much as possible of the above symmetries. The vertex-, edge-, polygon- and cell-centered clusters are of $I_h$, $D_{5h}$, $D_{3h}$, and $T_d$ symmetry, respectively. These four point groups are maximally compatible with, respectively, the four space-group-allowed point group symmetries, $T_h$, $C_{2v}$, $D_{3h}$ and $T_d$, point groups found in cubic, orthorhombic, hexagonal, and cubic crystals, respectively.

Not only should the space group have the above point group symmetries, there need be special sites within the unit cell, Wyckoff positions, which have these exact symmetries. For example, for the vertex-centered cluster, the Wyckoff site symmetry $T_h$ or $m\bar{3}$ is required. Possible space groups are therefore $Pm\bar{3}$, $Fm\bar{3}$, $Im\bar{3}$, $Pm\bar{3}n$, and $Fm\bar{3}c$. For cell-centered clusters, we need Wyckoff site symmetry $T_d$ or $\bar{4}3m$. Allowed space groups are $P\bar{4}3m$, $F\bar{4}3m$, $I\bar{4}3m$, $Pn\bar{3}m$, $Fm\bar{3}m$, and $Fd\bar{3}m$.

Crystalline examples of these clusters are found in $Al_6Mg_{11}Zn_{10}$, a 1:1 quasicrystalline approximant, and $Pt_5Zn_{21}$,[57,58] a $2\times2\times2$ superstructure of the γ-brass structure. Their unit cells, along with one example of the corresponding tetrahedral cluster, are shown in Figure 11. They crystallize in $Im\bar{3}$ and $F4\bar{3}m$ symmetry.

In exactly the same manner we can consider edge- and polygon-centered tetrahedral clusters. The list of space groups with $C_{2v}$ Wyckoff site symmetry is too long to list here. For the polygon-centered cluster with $D_{3h}$, either of $\bar{6}m2$ or $\bar{6}2m$ symmetry, the list of possible space groups include $P\bar{6}m2$, $P\bar{6}2m$, $P6/mmm$, $P6_3/mcm$, and $P6_3/mmc$. Neither rhombohedral nor cubic crystal space groups are compatible with Wyckoff site $D_{3h}$ symmetry. Examples of crystal structure with edge- or polygon-centered tetrahedral clusters are the $Mn_{10}Al_{29}$[59] decagonal quasicrystalline approximant and the $EuSr_2Mg_{13}$[60] structure. Their structures, with one example each of the corresponding tetrahedral cluster, are shown in Figure 11. These two crystals crystallize in, respectively, the *Pnma* and $P6_3/mmc$ space groups.

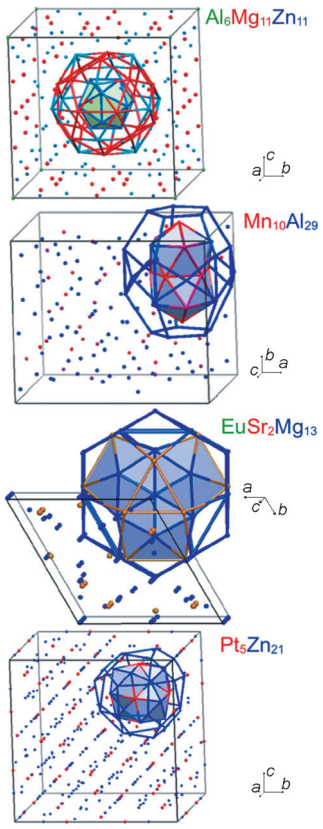


Figure 11. $Al_6Mg_{11}Zn_{11}$, $Mn_{10}Al_{29}$, $EuSr_2Mg_{13}$, and $Pt_5Zn_{21}$ unit cells. Elements are color-coded: mixed sites are denoted by the corresponding color mixtures: blue-green and green-red mixtures appear as turquoise and brown, respectively. For each structure, a single vertex-, edge-, polygon-, and cell-centered cluster is shown. The inner shell is represented as a filled polyhedron. Atoms at the centers of the polyhedra determine the colors of the polyhedral faces. Outer shell is shown in a ball-and-stick format.

Not only do these crystal structures show clear examples of the vertex-, edge-, polygon-, and cell-centered tetrahedral packing, they show as well marked pseudo-fivefold diffraction symmetry. The pseudo-fivefold diffraction images are themselves in the directions of the most central edges of the respective clusters. For the cubic $Pt_5Zn_{21}$ and hexagonal $EuSr_2Mg_{13}$ structures, the innermost cluster edges link, respectively, *IT* to *IT* atoms, the ⟨110⟩ real lattice directions, and *ITr* to *ITr* atoms, the real space ⟨100⟩ or equivalently the reciprocal space $\{2\bar{1}0\}$ directions.

In Figure 12 we therefore show the diffraction images orthogonal to the cubic $[1\bar{1}0]$ and hexagonal [100] directions. Our interest here is only with the strongest diffraction peaks. Within the Cerius$^2$ suite of programs,[61] we can filter

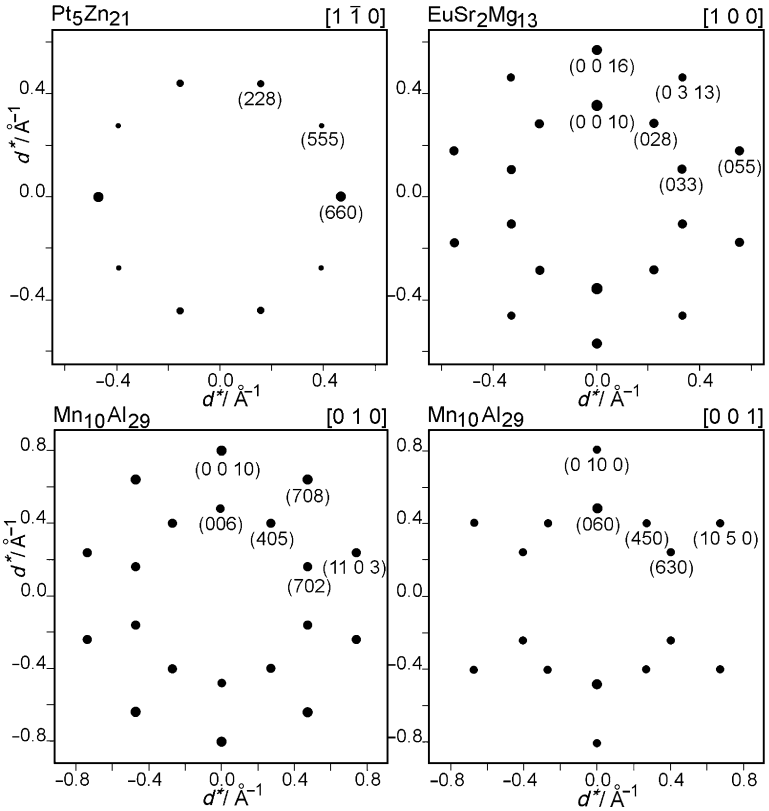


Figure 12. Diffraction pattern for the cell-centered $Pt_5Zn_{21}$, polygon-centered $EuSr_2Mg_{13}$, and edge-centered $Mn_{10}Al_{29}$ crystals along the indicated directions. For $Mn_{10}Al_{29}$, the [0 1 0] and [0 0 1] directions correspond, respectively, to *CE–CE* and *PG–PG*. The latter pattern shows less-marked pseudo-fivefold symmetry but its relation to the formers pseudo-fivefold symmetry is evident. Cerius[2] Intensity Factors: 0.15 ($Pt_5Zn_{21}$); 0.04 ($EuSr_2Mg_{13}$); 0.04 ($Mn_{10}Al_{29}$, [0 1 0]); 0.05 ($Mn_{10}Al_{29}$, [0 0 1]) A comparison of diffraction images with uniform intensity factors is shown in Supporting Information.

out weaker peaks by applying an Intensity Factor. With this filter, as Figure 12 shows, both crystals show marked rings of tenfold pseudosymmetric diffraction in the above specified directions. Such rings correspond to pseudo-fivefold rotational symmetry. The $Pt_5Zn_{21}$ and $EuSr_2Mg_{13}$ show, respectively, one and two such 10-fold rings. $Pt_5Zn_{21}$ has an inner ring and $EuSr_2Mg_{13}$ has inner and outer rings whose $d_{hkl}$, respectively, are approximately 2.1 and 2.7/1.7 Å.

In the case of the edge-centered cluster-based structure $Mn_{10}Al_{29}$, the most central edge connects the two *CE* sites to one another. As Figure 12 shows, this *CE-CE* direction, which in $Mn_{10}Al_{29}$ runs in the [010] real space lattice direction, has excellent pseudo-fivefold symmetry associated with it.

For edge-centered crystal structures, even the second-most central edge lies sufficiently near the projected-cluster center, a kind of pseudo-fivefold diffraction ring can be observed. These second-most central edges connect *PG* to *PG* sites. There are five different *PG–PG* directions, only one of which is orthogonal to a numerically simple real space direction. For $Mn_{10}Al_{29}$ one of the five *PG–PG* edges lies in the [001] real space direction, the other four *PG–PG* directions corresponding to 72 and 144° rotations of this direction. As Figure 12 shows, pseudo-fivefold diffraction along this axis is significantly distorted, but its relation to the better *CE–CE* pseudo-fivefold diffraction symmetry, also shown in this figure, is evident.

For diffraction images orthogonal to less simple real-space directions, relatively few diffraction reflections are *exactly* orthogonal to real-space lattice directions. Standard diffraction images that show all diffraction reflections orthogonal to a given real space lattice direction (this real-space direction is called the zone axis) fail, therefore, to capture pseudo-symmetry properly.

It is easiest in such cases to generate somewhat artificial diffraction images. We do so by choosing a crystallite size, where the crystallite center is chosen to be one of the four types of tetrahedral clusters. We choose crystallites which are 30 Å in diameter, centered around a high symmetry point of the crystal structure. The small size leads to significant dispersion around each (*hkl*) reflection. Contour maps orthogonal to a given real-space direction therefore can capture the intensity of reflections which do not exactly lie within the orthogonal plane.

Such crystallite diffraction images can be used to assess the pseudo-fivefold symmetries. We consider the vertex-cluster based $Al_6Mg_{11}Zn_{11}$ structure. In this structure we choose a zone axis in the ⟨503⟩ real-space directions, directions which correspond in real space to *CC–II* edges. Figure 13

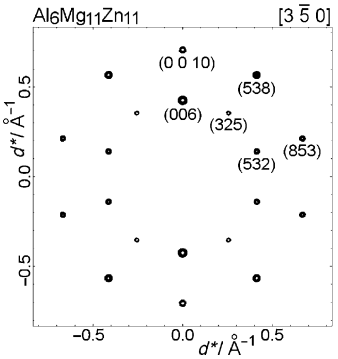


Figure 13. Diffraction pattern for a cluster-centered 3.0 nm diameter spherical crystallite of the vertex-centered $Al_6Mg_{11}Zn_{11}$ structure shown along the [3 5̄ 0] direction. Only peaks whose peak height is 0.27 times the most intense peaks are shown.

shows the marked pseudo-fivefold symmetries with respect to these zone axes.

**Smaller crystalline examples**: The four crystals considered in the previous section, $Al_6Mg_{11}Zn_{11}$, $Mn_{10}Al_{29}$, $EuSr_2Mg_{13}$, and $Pt_5Zn_{21}$, have Pearson symbols of *cI*162, *oP*156, *hP*96, and *cF*416, respectively. Based on the Wyckoff site symmetry of their corresponding space groups these four crystals can have two, four, two, and sixteen tetrahedral clusters, respectively, the cluster edges of which correspond to chemical bonds. As the vertex-, edge-, polygon-, and cell-centered tetrahedral clusters have 45, 44, 50, and 54 atoms, respectively, the tetrahedral clusters can account for, 90, 176, 100, and 864 potential sites, respectively.

In the previous examples, the number of atoms in a unit cell are therefore always within a factor of two of the number of atoms in the tetrahedral clusters themselves. In this section we turn to tetrahedral cluster crystals with just tens of atoms in their unit cells, unit cells one-quarter to one-tenth the size of the previous unit cells. These small unit cells nonetheless fashion centered clusters the same size as were found previously. Unit cells with just tens of atoms must lead to clusters forty to fifty atoms in size.

In one case noted below, a cubic crystal with a primitive unit cell of just six atoms generates a full inner-shell cell-centered 26-atom cluster as well as over half the outer shell. In this, as well as the other examples, atoms in the inner shell of one cluster belong to outer shells, and even the inner shells, of neighboring clusters. As may be expected, while some of our examples are able to create full inner- and outer-shelled tetrahedral clusters, in other examples, the tetrahedral clusters are imperfect: sites in the outer shell are found missing.

Small-sized unit cells for the vertex- and edge-centered clusters include $Mg_2Zn_{11}$[62] (*Pm*$\bar{3}$, *cP39*) and $Cd_2Cs_5Tl_{11}$[63] (*Amm*2, *oA36*), with, respectively, one and two clusters per unit cell. The unit cells in both cases are smaller than a single centered cluster. Illustrations of these structures are shown in Figures 14 and 15. In both these examples, both inner and outer shells are fully present. With their small unit cell sizes, their diffraction images, see Figures 16 and 17, show only partially discernible pseudo-fivefold diffraction symmetry.

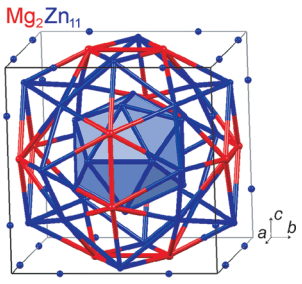


Figure 14. $Mg_2Zn_{11}$ unit cell. Elements are color-coded and a single vertex-centered cluster is shown. Inner and outer shells are represented, respectively, in filled-polyhedron and ball-and-stick formats. The polyhedral faces are blue as a Zn atom lies at the cluster center.

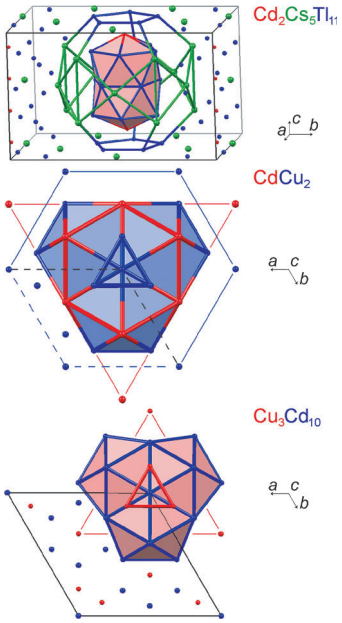


Figure 15. $Cd_2Cs_5Tl_{11}$, $Cu_3Cd_{10}$ and $CdCu_2$ unit cells. Elements are color-coded. For each structure a single edge- or polygon-centered cluster is shown. The inner shell is represented as a filled polyhedron, whose face is colored according to the central site element type. Outer shell is shown in a ball-and-stick format. $Cu_3Cd_{10}$ and $CdCu_2$ outer shells are incomplete: to aid the eye *OTr* or *FlPr and HgPr* sites are joined by thin lines. Where necessary for clarity, the unit cell is therefore indicated with dotted lines. $CdCu_2$ has the $MgZn_2$ structure type.

Small-celled examples of the polygon-centered cluster include both the ubiquitous hexagonal Laves phase $MgZn_2$[64] (*hP12*) and the slightly larger $Co_2Al_5$ (*hP28*)[65,66] structure. As in the later section of this paper, we will consider the Cu–Cd phase diagram, we illustrate here $CdCu_2$, a $MgZn_2$-type structure and $Cu_3Cd_{10}$, a $Co_2Al_5$-type system. Illustrations of their unit cells showing their polygon-centered tetrahedral clusters are given in Figure 15.

In $CdCu_2$, the full inner shell of the cluster is present. But with only twelve atoms in the primitive unit cell, it proves impossible to re-create fully the complete outer shell. Of the four outer shell sites, the *ElPr*, *FlPr*, and *HgPr* are present while the *OTr* is not. Similarly in $Cu_3Cd_{10}$, while the full inner shell is present, only the *ElPr* and *OTr* sites are present in the outer shell. Nonetheless, as Figure 16 shows, their diffraction images have excellent pseudo-fivefold symmetry.

The situation for cell-centered clusters is more complicated. The issue is not that cell-centered tetrahedral clusters are rare; they are in fact quite common. Both the ubiquitous Laves phase $MgCu_2$ (*cF24*)[67] and the important γ-brass structure (*cF52*), a structure found in $Cu_5Cd_8$,[68] are based on cell-centered tetrahedral clusters. Figure 18 shows both contain the full inner shell cell-centered cluster. γ-brass and $MgCu_2$ contain, respectively, the full and over half the outer shell of this same cluster. The complication is not in their structures but their diffraction images.

In Figure 19 we show diffraction images for three different noble-metal-rich $MgCu_2$-type structures, $YNi_2$,[69,70]

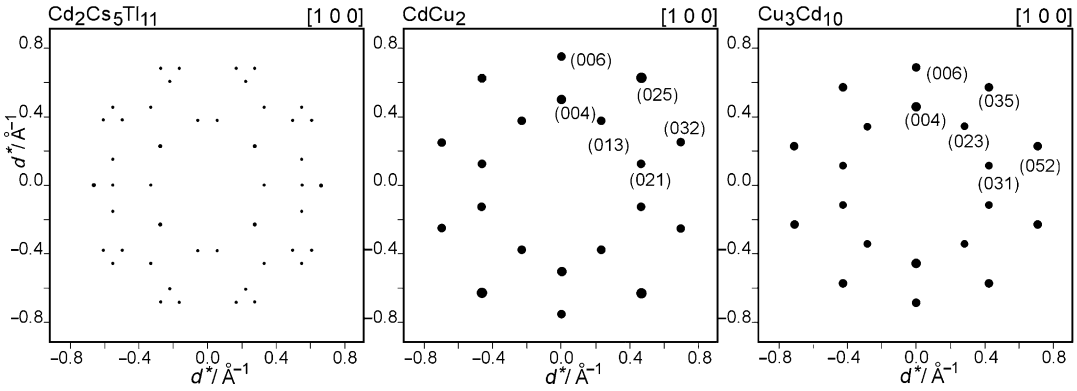


Figure 16. Diffraction pattern for the edge-centered $Cd_2Cs_5Tl_{11}$ and polygon-centered $CdCu_2$ and $Cu_3Cd_{10}$ crystals along the [1 0 0] direction. For the latter two crystals, pseudo-fivefold symmetry is clear, in the former system the pseudosymmetry is less-marked. Less evident pseudosymmetry is often found in tetrahedral-packed crystals with small unit cells. Cerius$^2$ intensity factors: 0.100 ($Cd_2Cs_5Tl_{11}$); 0.040 ($CdCu_2$); 0.040 $Cu_3Cd_{10}$. A comparison of diffraction images with uniform intensity factors is shown in the Supporting Information.

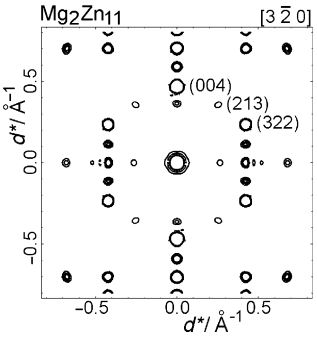


Figure 17. Diffraction pattern for a cluster-centered 1.5 nm diameter spherical crystallite of the vertex-centered $Mg_2Zn_{11}$ structure shown along the [3 $\bar{2}$ 0] direction. The weak intensity of the {2 1 3} reflection in this Figure is the result of this reflection's considerable distance from the plane normal to the [3 2 0] direction. Only peaks whose peak height are $\geq$0.10 times the most intense peaks are shown.

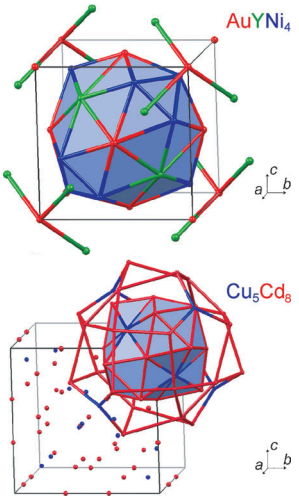


Figure 18. $AuYNi_4$ and $Cu_5Cd_8$ unit cells. Elements are color-coded. For each structure a single cell-centered cluster is shown. The inner shell is represented as a filled polyhedron, whose face is colored according to the central site element type. While $Cu_5Cd_8$ has the full outer shell, $AuYNi_4$ has only the *ExT* and *GrTt* outer-shell sites. The $AuYNi_4$ is related to the $MgCu_2$ structure type, where Au and Y lie in the latter Mg sites. $Cu_5Cd_8$ has the γ-brass structure.

$AuYNi_4$,[71] and $ScNi_2$.[72] (We choose these three as representative examples of noble-metal-rich Laves phases, noble metals being one focus of this paper.) For the first two, imperfect pseudo-fivefold rings composed of members of the {222}, {311}, and {220} sets of reflections are evident. In the third, $ScNi_2$, the {220} peak is absent, while {400} is now present and the sense of the pseudo-fivefold symmetry is lost. Chemically it seems evident that scandium and yttrium play similar roles in, respectively, $YNi_2$ and $ScNi_2$, but diffraction images depend on total vs. valence electron densities and Y and Sc differ significantly from one another. This result indicates a shortcoming in using diffraction images to elucidate structural stability trends.

The situation with the diffraction pattern of γ-brass structure is even more complex. It can be understood if we refer back to the $Pt_5Zn_{21}$ structure, a $2\times2\times2$ superstructure of γ-brass. While γ-brass contains two symmetry equivalent polygon-centered tetrahedral clusters in an *I*-centered cell, the $Pt_5Zn_{21}$ structure has sixteen such clusters based on four crystallographically different polygon-centered clusters in a face-centered cell.

As shown previously, the $Pt_5Zn_{21}$ has pseudo-fivefold symmetry in the ⟨110⟩ directions. Connected to one another by a pseudo-fivefold rotation along these directions are the (660), (822), and (555) reflections. In going from the $Pt_5Zn_{21}$ super-structure to the parent γ-brass type, the real unit cell halves in each axis direction as do the (*hkl*) indices. The $Pt_5Zn_{21}$ (660), (822), and (555) reflections therefore correspond to the γ-brass (330), (411), and $(2\frac{1}{2}2\frac{1}{2}2\frac{1}{2})$ reciprocal space vectors. Of these latter three directions, only the first two are composed of whole number indices and can correspond to γ-brass reflections. Of the four whole-numbered peaks closest to the $(2\frac{1}{2}2\frac{1}{2}2\frac{1}{2})$ direction, that is, the (222), (322), (332), and (333) directions, only the (222) and (332) peaks are observed; (333) and (322), both having $h+k+l=$

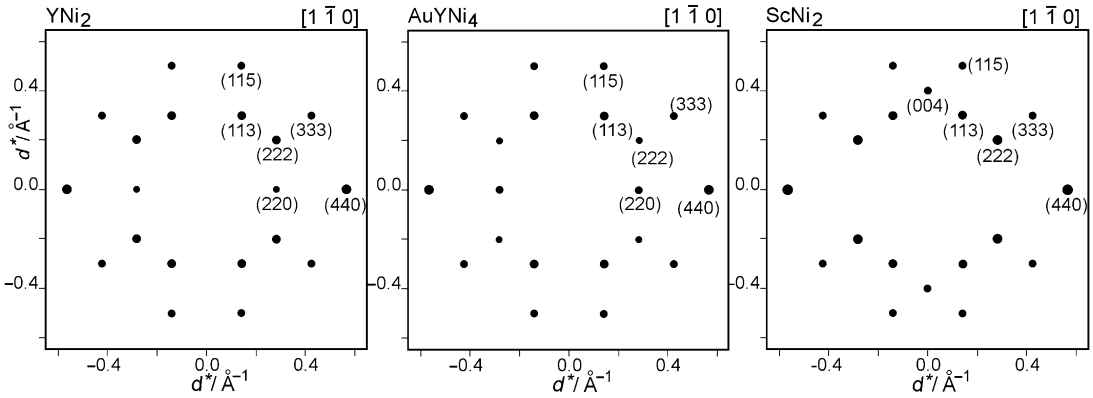


Figure 19. Diffraction pattern for cell-centered $YNi_2$, $AuYNi_4$ and $ScNi_2$ crystals along the [1 $\bar{1}$ 0] direction. All three structures are related to the $MgCu_2$ Laves structure. Pseudo-five-fold symmetry is clear in the first two structures but not the third. Cerius$^2$ intensity factors: 0.040 ($YNi_2$); 0.030 ($AuYNi_4$); 0.040 ($ScNi_2$). A comparison of diffraction images with uniform intensity factors is shown in the Supporting Information.

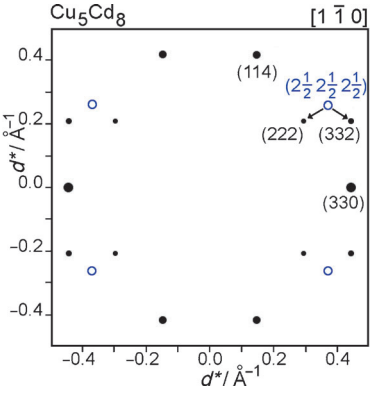


Figure 20. Diffraction pattern for the γ-brass-type $Cu_5Cd_8$ along the [1 $\bar{1}$ 0] direction. Five-fold rotations applied to either the (3 3 0) and (4 1 1) peaks would result in a $(2\frac{1}{2}2\frac{1}{2}2\frac{1}{2})$ peak, a direction not permitted in diffraction. The disallowed $(2\frac{1}{2}2\frac{1}{2}2\frac{1}{2})$ location is shown as a blue open circle (see Supporting Information). Diffraction occurs instead at (2 2 2) and (3 3 2), the two closest locations where diffraction is symmetry allowed. Cerius$^2$ intensity factor is 0.45.

$2n+1$, are systematically absent in the *I*-centered γ-brass structure.

In the case of γ-brass, five-fold pseudo-rotations along the ⟨110⟩ directions therefore lead to four symmetrically equivalent sets of reciprocal space vectors, {330}, {411}, {222}, and {332}. (A fifth, the {422}, will also prove equally significant in a later section of the paper.) Figure 20 shows the diffraction pattern orthogonal to the ⟨110⟩ direction for $Cu_5Cd_8$, a γ-brass structured member of the Cu–Cd phase diagram. As anticipated, these four sets of reflections are the four principal sets present in this diffraction pattern. However, although we can understand that this diffraction image as being derived from pseudo-five-fold symmetry, as this Figure shows, the pseudosymmetry itself is not easy to see.

**Larger crystalline examples**: So far we have considered crystals whose unit cells are either roughly the same size or are even smaller than the size of individual tetrahedral clusters. We can, however, consider unit cells where the Pearson symbol denotes a unit cell significantly greater in size than can be accounted for by potential tetrahedral cluster sites. We could suppose that such larger crystalline structures are projections of four-dimensional objects larger than the 600-cell.

As we and others have shown, these larger objects are often 4D quasicrystals,[43,47] but these quasicrystals have the same 4D point group symmetry as the 600-cell itself. In such cases, the fivefold rotational symmetry corresponding to the 720 edges of the 600-cell, retain their character as fivefold pseudosymmetry axes in their large crystal unit cell 3D projections. In other words, even in very large 3D crystal structures, we do not have to delve beyond the 600-cell symmetries in order to understand 3D pseudosymmetries. Just as a cube or an octahedron can be used to understand the rotational symmetries of 3D cubic-unit-celled crystals such as rock salt or perovskite, the 600-cell can be used to understand the point group symmetries of 4D quasicrystals.

In looking for examples of such phases, we look for clusters which have the same point group symmetry as the projected 600-cell and whose diffraction images show the same pseudo-fivefold symmetry axes. In this section we consider just the inner shell of the four centered tetrahedral crystals, this shell being enough to define the overall point group symmetry. We relax the previous restriction that these inner shells have chemical bond edge lengths. Indeed, tetrahedral edge lengths longer than a chemical bond are more in keeping with these crystals' large unit cells.

Examples of such larger crystal structures are the $SiMn_6Pd_{23}Al_{70}$,[73] $Pd_3Al_7$,[74] $MnAl_4$,[75,76] and $Cd_3Cu_4$ structures with Pearson symbols of *cP*597, *oP*328, *hP*574, and *cF*1124. These unit cells are roughly double the size of the original crystals discussed in this paper. Their crystal structures and their respective vertex-, edge-, polygon-, and cell-centered tetrahedral clusters are shown in Figure 21. Shown in Figures 22 and 23 are their corresponding diffraction images along, respectively, the inner-shell central-edge *CC–II*, *CE–CE*, *ITr–ITr*, and *IT–IT* directions.

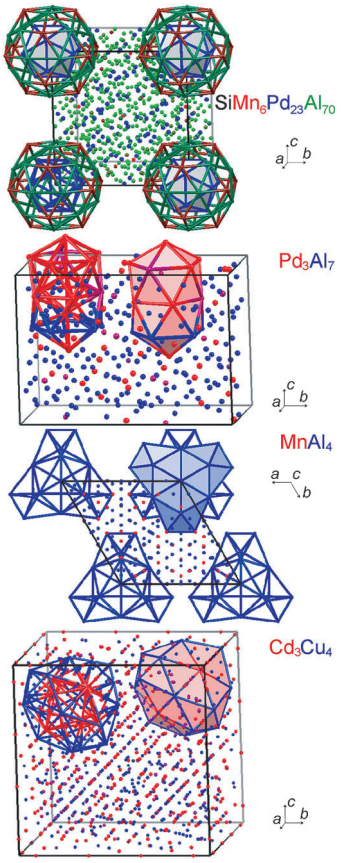


Figure 21. Vertex-centered $SiMn_6Pd_{23}Al_{70}$, edge-centered $Pd_3Al_7$, polygon-centered $MnAl_4$, and cell-centered $Cd_3Cu_4$ unit cells. Elements are color-coded. Mixed sites are denoted by the corresponding color mixtures: green-red mixtures appear as brown. Only a few of the possible tetrahedral clusters are shown. For $SiMn_6Pd_{23}Al_{70}$, the illustrated cluster contains both inner and outer shells; for the remaining cases only the inner shell is illustrated. Due to the large unit cell sizes, chosen here are clusters whose edges correspond to atoms spaced roughly $\tau$ further apart than regularly bonded metal atoms.

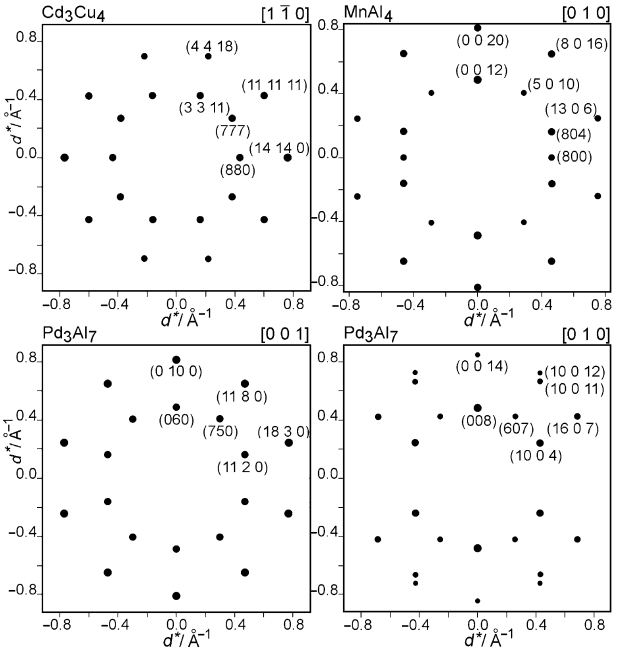


Figure 22. Diffraction patterns for the cell-centered $Cd_3Cu_4$, polygon-centered $MnAl_4$, and edge-centered $Pd_3Al_7$ crystals along the indicated directions. For $Pd_3Al_7$, the [0 0 1] and [0 1 0] directions correspond, respectively, to *CE–CE* and *PG–PG*. The latter pattern shows less-marked pseudo-fivefold symmetry but its relation to the former's pseudo-fivefold symmetry is evident. Cerius[2] intensity factors: 0.040 ($Cd_3Cu_4$); 0.060 ($MnAl_4$); 0.060 ($Pd_3Al_7$); 0.080 ($Pd_3Al_7$). A comparison of diffraction images with constant intensity factors is shown in the Supporting Information.

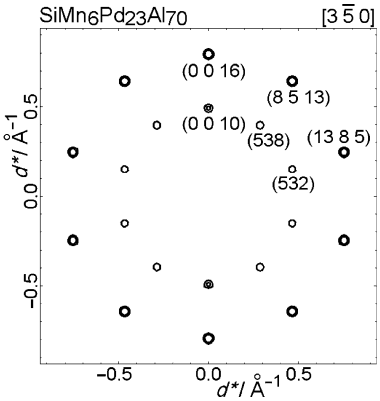


Figure 23. Diffraction pattern for a cluster-centered 3.0 nm diameter spherical crystallite of the vertex-centered $SiMn_6Pd_{23}Al_{70}$ structure shown along the [3 $\bar{5}$ 0] direction. Only peaks whose peak height are $\geq$0.29 times the most intense peaks are shown.

Not surprisingly, both the vertex-centered cluster $SiMn_6Pd_{23}Al_{70}$ structure and the cell-centered cluster $Cd_3Cu_4$ structure, with their large unit cells, reveal excellent pseudo-fivefold diffraction. The polygon-centered $MnAl_4$ shows an extra principal spot in its inner-most ring, the {800} set of reflections. In the next two sections we explain the origin of this spot. As we shall see, this extra set of reflections is a direct consequence of pseudo-fivefold symmetry. Finally, in the edge-centered cluster $Pd_3Al_7$ structure, the *CE–CE* and one of the *PG–PG* edges run in, respectively, the [001] and [010] directions. While the pseudo-fivefold symmetric nature of the former pattern is the more marked, the relation between the two patterns is evident.

**Cluster edges and diffraction**: Central edges in the vertex-, edge-, polygon-, and cell-centered tetrahedral clusters are pseudo-fivefold rotation diffraction symmetry axes. But they play an additional significant role in diffraction. This role can only be understood if we recognize that tetrahedral cluster edges can be used to define plane waves, and not just any plane waves, but in fact the strongest diffracting plane waves.

The plane waves defined by a cluster edge are plane waves whose directions of travel are exactly the same as given cluster edge bond-directions and whose wavelengths can be deduced from the cluster edge bond lengths. Such wavelengths must be deduced by taking into account not just the actual cluster edge distances, but how these edges

orient themselves in optimal directions away from the center of the projection. As Figure 24 shows, the actual edge distances, shown in this Figure as a red barbell, are always greater than the apparent wavelengths, shown as black arrows. For example, we can consider a central cluster edge of, respectively, the $Al_6Mg_{11}Zn_{11}$ and $Pt_5Zn_{21}$ structures. The former is a vertex-based and the latter a cell-based cubic structure. Representative central edges are therefore, respectively, *II–II* and *IT–IT* edges.

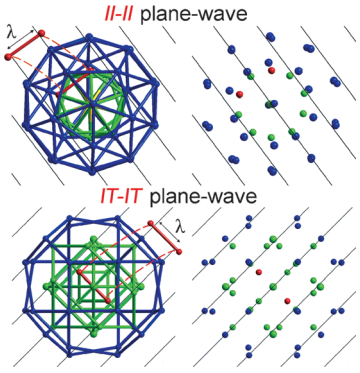


Figure 24. Top row: 45-atom vertex-centered cluster from the $Al_6Mg_{11}Zn_{11}$ structure together with the plane wave corresponding to an *II–II* edge. Bottom row: a 54-atom cell-centered cluster from the $Pt_5Zn_{21}$ structures together with the plane wave corresponding to an *IT–IT* edge. Inner and outer shells are color coded. *II* and *IT* sites are shown in red. Both plane waves exhibit strong constructive interference with the projected clusters.

But, as we have found previously, all cluster edges are pseudosymmetric to one another. If one *II–II* and one *IT–IT* edge-based plane wave have strong constructive interference, then all the other cluster edge-based plane waves will also have similar constructive interference. Edges closest to the cluster center, having the strongest pseudosymmetry, will naturally follow this principle the best. This fact allows for an unusual but powerful diffraction picture.

In this picture, we take the unusual step of constructing in *reciprocal* space a cluster fully similar to the inner-most shell of the real-space tetrahedral cluster. This inner-most shell contains all the cluster edges which correspond to the most constructive interference. But as this new cluster is given in reciprocal space, these cluster edges are given in the form of reciprocal space vectors. As such edges correspond to strong constructively interfering plane waves, such a Figure gives a pictorial representation of the strongest diffraction peaks.

We form such reciprocal-space clusters using crystalline reciprocal-space unit cell axes. In Figure 25 we do so for $SiMn_6Pd_{23}Al_{70}$ the largest unit-celled vertex-centered tetrahedral crystal structure discussed in this paper. The inner shell of this structure consists of the *CC* site located at the origin and the twelve *II* sites located on all even permutations of ($\pm 8\,0\,\pm 5$), a total of thirteen positions in all.

Between these thirteen vertices are forty-two edges: twelve *II–CC*, and thirty *II–II* edges. As the Figure shows

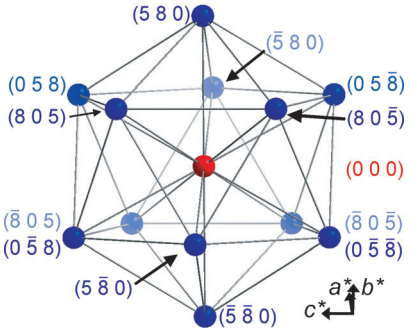


Figure 25. Inner shell of a vertex-centered-projected reciprocal-space 600-cell using $SiMn_6Pd_{23}Al_{70}$ reciprocal space axes as a coordinate basis. The strongest diffraction peaks for the $SiMn_6Pd_{23}Al_{70}$ crystal correspond to first and second nearest neighbor vectors derived from this reciprocal space cluster, see Table 1.

the former edges form the {8 0 5} while the latter are made up of the twenty-four {8 5 3} and the six {10 0 0}. Also relevant to this discussion will be second nearest neighbor pairs of sites, sites which lie on opposite sides of cluster triangular faces. There are thirty second-nearest-neighbor pairs of sites: the twenty-four {13 8 5} and the six {16 0 0}. These second nearest neighbors may also be deduced from the figure.

In Table 1, we show in descending order of intensity all the strongest diffraction peaks for the $SiMn_6Pd_{23}Al_{70}$ structure. This list is based on all diffraction peaks with $d_{hkl}$ up to 1.14 Å, a value which corresponds to a $Cu_{K\alpha 1}$ $2\Theta$ value of 85°. Remarkably, the five strongest peaks in this entire structure are exactly the peaks which can be generated from the inner shell of the reciprocal lattice tetrahedral cluster.

In many structures, the most strongly diffracting peaks are (*hkl*) with low numerical indices, reflections like (100) or (110). For tetrahedrally-packed structures, the strongest peaks correspond to cluster edges. Taking into account reflection multiplicities, they form the two 10-fold rings shown in Figure 22; they number 72 reflections in total.

Table 1. Strongest (*hkl*) in $SiMn_6Pd_{23}Al_{70}$.

| (*h k l*) | $d_{hkl}$ [Å][a] | Multiplicity | Vertex–vertex (*k*-space-coord.) | Vertex–vertex (atom sites) | Intensity[b] |
|---|---|---|---|---|---|
| (8 0 5) | 2.14[c] | 12 | (8 0 5)–(0 0 0) | *II–CC* | 100.0 |
| (10 0 0) | 2.02 | 6 | (5 8 0)–(5̄ 8 0) | *II–II* | 69.0 |
| (8 5 3) | 2.04 | 24 | (8 0 5̄)–(0 5̄ 8̄) | *II–CC* | 57.5 |
| (13 8 5) | 1.26[d] | 24 | (8 0 5)–(5̄ 8̄ 0) | *II–II* | 56.5 |
| (16 0 0) | 1.26 | 6 | (8 0 5)–(8̄ 0 5) | *II–II* | 53.8 |
| (5 0 3) | 3.47 | 12 | (13 0 8)–(8 0 5) | *OI–II*[e] | 38.8 |
| (1 0 0) | 20.21 | 6 | – | – | 21.5 |
| (5 3 2) | 3.28 | 24 | – | – | 7.0 |

[a] Table includes $d_{hkl}$ of up to 1.14 Å, corresponding to $Cu_{K\alpha 1}$ $2\theta$ of 85°. [b] Intensity is based on powder diffraction data from the Cerius[2] suite of programs but is given per reflection, with neither atomic Debye–Waller nor Lorentz-polarization factors included. [c] Inner shell edges have $d_{hkl}$ ranging from 2.0 to 2.2 Å. [d] Inner shell second nearest neighbors have $d_{hkl}$ ranging from 1.2 to 1.3 Å. [e] *OI* is located at {13 0 8} while *DH* is at {8 8 8} and {13 5 0}.

In this table first nearest neighbor edges and second nearest neighbor pairs of capping atoms can be readily distinguished from one another. First and second nearest neighbors have, respectively, $d_{hkl}$ ranging from 2.0 to 2.1 Å and 1.2 to 1.3 Å. As needs be in a tetrahedrally packed icosahedral structure, these $d_{hkl}$ are approximately related to one another by $\tau$, the golden mean, as is expected in all tetrahedrally packed icosahedral structures, $\tau \approx 2.04/1.26$.

**Examples of reciprocal-space diffraction clusters**: In exactly the same manner we can consider edge-, polygon-, and cell-centered tetrahedral-structures. We begin with the highest symmetry of the three remaining clusters, the cell-centered type. In Table 2 we list the strongest reflections in the $Cd_3Cu_4$ system, a phase with cell-centered clusters. Just as in the $SiMn_6Pd_{23}Al_{70}$ case, the strongest diffraction peaks are found in two rings at, respectively, $d_{hkl}$ from 2.1–2.3 and 1.3–1.4 Å.

Table 2. Strongest (*hkl*) in $Cd_3Cu_4$.

| (*h k l*) | $d_{hkl}$ [Å][a] | Multiplicity | Vertex–vertex (*k*-space-coord.) | Vertex–vertex (atom sites) | Intensity[b] |
|---|---|---|---|---|---|
| (8 8 0) | 2.29[c] | 12 | (4 4 4)–($\bar{4}$ $\bar{4}$ 4) | *IT–IT* | 100.0 |
| (11 3 3) | 2.19 | 24 | (4 $\bar{4}$ $\bar{4}$)–($\bar{7}$ $\bar{7}$ $\bar{7}$) | *IT–OT* | 88.8 |
| (14 14 0) | 1.31[d] | 12 | (7 7 $\bar{7}$)–($\bar{7}$ $\bar{7}$ $\bar{7}$) | *OT–OT* | 80.6 |
| (7 7 7) | 2.13 | 8 | (7 $\bar{7}$ 7)–(0 $\overline{14}$ 0) | *OT–OH* | 75.6 |
| | | | (7 7 $\bar{7}$)–(0 0 $\overline{14}$) | *OT–OH* | |
| | | | ($\bar{7}$ 7 7)–($\overline{14}$ 0 0) | *OT–OH* | |
| (11 11 11) | 1.36 | 8 | (4 4 4)–($\bar{7}$ $\bar{7}$ $\bar{7}$) | *IT–OT* | 67.5 |
| (18 4 4) | 1.37 | 24 | (4 4 4)–($\overline{14}$ 0 0) | *IT–OH* | 34.6 |
| (10 4 4) | 2.25 | 24 | (14 0 0)–(4 $\bar{4}$ $\bar{4}$) | *OH–IT* | 25.3 |
| (7 7 1) | 2.60 | 24 | – | – | 11.3 |
| (12 2 2) | 2.10 | 8 | – | – | 10.2 |

[a] Table includes $d_{hkl}$ of up to 1.14 Å, corresponding to $Cu_{K\alpha 1}$ $2\theta$ of 85°. [b] As in Table 1, intensity is given per reflection, with neither atomic Debye–Waller nor Lorentz-polarization factors included. [c] Inner shell edges have $d_{hkl}$ ranging from 2.1 to 2.3 Å. [d] Inner shell second nearest neighbors have $d_{hkl}$ ranging from 1.3 to 1.4 Å.

In Figure 26 and Table 2 we analyze these diffraction peaks using a reciprocal-space tetrahedral cluster, like the one used in the previous section but now cell-centered rather than vertex-centered. Just as in the previous example, we find all strong diffraction peaks correspond to vectors connecting the reciprocal-space cluster first or second nearest neighbors. First nearest neighbor reflections break into four sets, the {8 8 0}, {11 11 3}, {7 7 7}, and {10 4 4} reflections, a total of 68 different reflections (68 = 12 + 24 + 8 + 24). Second nearest neighbors break into another three sets, the {14 14 0}, {11 11 11}, and {18 4 4} reflections, a total of 44 additional directions.

The diffraction intensity of the first nearest neighbor reflections will prove to be, in later sections of this paper, significant for phase stability. Their intensities therefore merit close examination. In Table 2 we see, in cell-centered clusters, that *IT–IT* reflections are the strongest, closely followed by the *IT–OT* reflections. By contrast both *OT–OH* and *IT–OH* peaks are weaker.

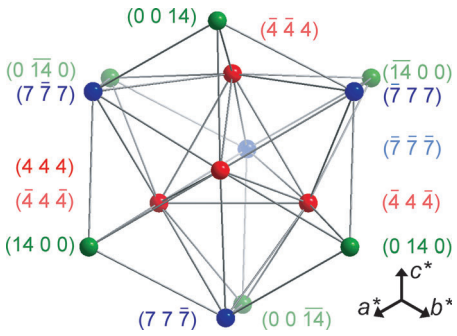


Figure 26. Three most central sites (*IT*, *OT*, and *OH*) of a cell-centered-projected reciprocal-space 600-cell using $Cd_3Cu_4$ reciprocal-space axes as a coordinate basis. The strongest diffraction peaks for the $Cd_3Cu_4$ crystal correspond to first and second nearest neighbor vectors derived from this reciprocal-space clusters, see Table 2.

If we recall the concept of the hierarchy of edges presented earlier in this paper (Figure 10) we rationalize the more intense character of the former pair of edges as they are more centrally placed than the latter pair. But that noted, Table 2 does present the reader with an additional puzzle. In this table the *OT–OH* peaks are shown to have an intensity three times stronger than the *IT–OH* peaks. From the point of view of the hierarchy of edges, this is surprising as the *IT–OH* and *OT–OH* edges are both roughly equidistant from the cluster center.

Table 2 together with Figure 26 accounts for this threefold variation. Figure 26 shows three *OT* vertices nearly eclipsing three *OH* vertices. The three eclipsing pairs of *OH* and *OT* sites are actually related to one another by exactly the same reciprocal lattice vector, {7 7 7}, see Table 2. Apparently edge reflection intensity is best understood on a per edge basis. *OT–OH* edge reflection intensities therefore need to be divided by three, as they are shared amongst three edges. With this correction factor *IT–OH* and *OT–OH* edges are nearly equal in intensity.

Our $Cd_3Cu_4$ system has reintroduced to us to the concept of the hierarchy of cluster edges. It has further introduced to us the concept of measuring intensity on a per edge rather than the per reflection basis ordinarily used to report single crystal diffraction data. Inner-most edges are the strongest. On a per edge basis the more central *IT–IT* and *IT–OT* edges are roughly four times as intense as either of the less central *IT–OH* or *OT–OH* edges.

We turn now to $MnAl_4$, a polygon-centered cluster structure. In Table 3 and Figure 27 we tabulate this structure's strongest diffraction peaks as well as a reciprocal-space polygon-centered cluster which can be used to interpret these intensities. As this Table and Figure show, the strongest diffraction peaks are found at $d_{hkl}$ of 2.0–2.2 and 1.2–1.3 Å, corresponding to the inner shell of first and second nearest neighbors of a reciprocal-space polygon-centered cluster. First nearest neighbors are found in seven symmetry types of reflections, a total of 74 = 2 + 12 + 6 + 6 + 24 + 12 + 12 directions. Second nearest neighbors comprise five symmetry types composed of 44 = 6 + 12 + 2 + 12 + 12 directions.

Table 3. Strongest (*hkl*) for $MnAl_4$.

| (*h k l*) | $d_{hkl}$ [Å][a] | Multiplicity | Vertex–vertex (*k*-space-coord.) | Vertex–vertex (atom sites) | Intensity[b] |
|---|---|---|---|---|---|
| (0 0 12) | 2.06[c] | 2 | (8 0 6)–(8 0 $\bar{6}$) | *IPr–IPr* | 100.0 |
| | | | (8 8 6)–(8 8 $\bar{6}$) | *IPr–IPr* | |
| | | | (0 $\bar{8}$ 6)–(0 $\bar{8}$ $\bar{6}$) | *IPr–IPr* | |
| (8 0 4) | 2.04 | 12 | (8 0 $\bar{6}$)–(0 0 $\overline{10}$) | *IL–IPr* | 63.5 |
| | | | (8 $\bar{8}$ 10)–(0 $\bar{8}$ 6) | *OPr–IPr* | |
| | | | (8 8 $\bar{6}$)–(0 8 $\overline{10}$) | *IPr–OPr* | |
| (8 8 0) | 1.25[d] | 6 | (0 8 10)–($\bar{8}$ 0 10) | *OPr–OPr* | 55.6 |
| (8 0 16) | 1.26 | 12 | (0 0 10)–(8 0 $\bar{6}$) | *IL–IPr* | 43.3 |
| (0 0 20) | 1.23 | 2 | (0 0 10)–(0 0 $\overline{10}$) | *IL–IL* | 38.9 |
| (5 5 0) | 2.00 | 6 | (0 5 0)–($\bar{5}$ 0 0) | *ITr–ITr* | 37.3 |
| (8 0 0) | 2.16 | 6 | (0 0 $\overline{10}$)–($\bar{8}$ 0 10) | *IL–OPr* | 36.1 |
| | | | (0 0 $\overline{10}$)–($\bar{8}$ 0 $\overline{10}$) | *IL–OPr* | |
| (5 3 6) | 2.12 | 24 | (5 $\bar{5}$ 0)–(0 $\bar{8}$ 6) | *ITr-IPr* | 32.0 |
| (5 0 10) | 2.01 | 12 | (0 0 10)–($\bar{5}$ 0 0) | *IL–ITr* | 30.1 |
| (13 0 6) | 1.27 | 12 | (8 0 6)–(5 0 0) | *IPr–ITr* | 25.8 |
| (0 0 4) | 6.17 | 2 | – | – | 24.0 |
| (3 0 10) | 2.27 | 12 | ($\bar{5}$ 0 0)- ($\bar{8}$ 0 10) | *ITr–OPr* | 13.8 |
| (8 5 10) | 1.30 | 24 | (0 5 0)–($\bar{8}$ 0 10) | *ITr–OPr* | 10.9 |
| (5 0 9) | 2.15 | 12 | – | – | 8.1 |

[a] Table includes $d_{hkl}$ of up to 1.14 Å, corresponding to $Cu_{K\alpha 1}$ $2\theta$ of 85°. [b] Intensity as in Table 1is given per reflection, with neither atomic Debye–Waller nor Lorentz-polarization factors included. [c] Inner shell edges have $d_{hkl}$ ranging from 2.0 to 2.2 Å. [d] Inner shell second nearest neighbors have $d_{hkl}$ ranging from 1.2 to 1.3 Å.

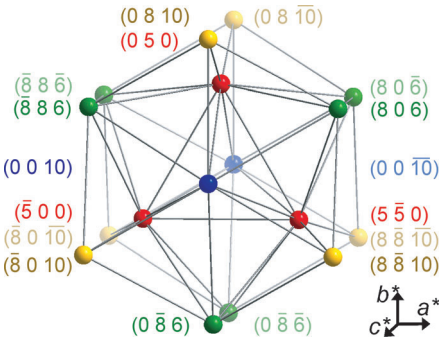


Figure 27. Four most central sites (*ITr*, *IL*, *IPr*, and *OPr*) of a polygon-centered-projected reciprocal-space 600-cell using $MnAl_4$ reciprocal space axes as a coordinate basis. The strongest diffraction peaks for the $MnAl_4$ crystal correspond to first and second nearest neighbor vectors derived from this reciprocal-space cluster, see Table 3.

As Table 3 shows, polygon-centered clusters contain more equivalent edges than cell-centered ones. For $MnAl_4$, three equivalence relations present themselves: triads of *IPr–IPr* edges point in the same direction as each other; *IL–IPr* edges point in the same direction as pairs of *IPr–OPr* edges; and finally pairs of *IL–OPr* edges point in the same direction.

With this understanding we turn to the first nearest neighbor reflections in Table 3, the strong reflections with $d_{hkl}$ ranging from 2.0 to 2.2 Å. On a per edge basis, edges between *ITr*, *IL*, and *IPr* prove to be the most central; they are uniformly the strongest. Their intensities range from 30–45%. Edges between one of these three more central sites and the more exterior *OPr* site, on a per edge basis are weaker and range from 14–18%, a factor of two to three weaker in intensity than the more central edges. We deduce for the {8 0 4} reflection, which is based on one central *IL–IPr* and two less central *IPr–OPr* edges, with a total intensity of 64%, that the *IL–IPr* edge has a weight of 30–45% while the *IPr–OPr* edges have a weight of 10–18%, their sum equalling the requisite total.

Only one type of centered reciprocal space tetrahedral cluster remains to be considered: the edge-centered one. We consider the $Mn_{10}Al_{29}$ structure here. Its reciprocal space edge centered cluster and this structure's most intense diffraction peaks are presented in Figure 28 and Table 4. As Table 4 shows, the twenty-two strongest reflections in this structure are first and second nearest neighbor vectors of the edge-centered reciprocal space cluster. First and second nearest neighbors have $d_{hkl}$ ranging from 2.0–2.3 and 1.2–1.35 Å, respectively.

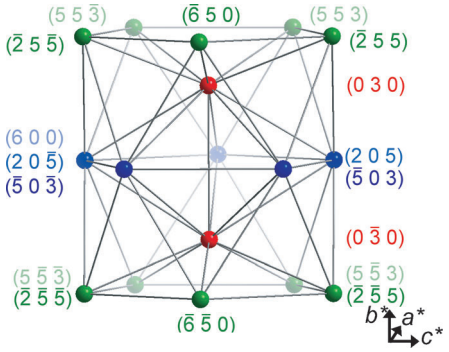


Figure 28. Three most central sites (*CE*, *PG*, and *PPr*) of an edge-centered-projected reciprocal-space 600-cell using $Mn_{10}Al_{29}$ reciprocal-space axes as a coordinate basis. The strongest diffraction peaks for the $Mn_{10}Al_{29}$ crystal correspond to first and second nearest neighbor vectors derived from this reciprocal-space cluster, see Table 4.

Turning just to first nearest neighbors, for edge-centered clusters, the only edge equivalence relations connect *PG–PG* to *PPr–PPr* edges. *PG–PG* sites lie in a pentagon, while the *PPr* sites form a pentagonal prism. As Figure 28 illustrates, the two pentagons of the pentagonal prism and the *PG* pentagon itself all have edges pointing in the same direction as one another. All *PG–PG* edges are therefore equivalent to two *PPr–PPr* edges.

With this understanding, we consider diffraction intensities. The central most edge in the edge-centered cluster is *CE*, the *CE–CE* edge is therefore strongest and in Table 4 is set at 100% intensity. Edges involving the *CE* and the somewhat less central *PG* have intensities from 50–70%. *PPr* sites are significantly less central than *PG* sites and edges involving a *PPr* site coupled to a *CE* or *PG* edges have intensities range from 21–47%. In summary, the reciprocal-space edge-centered tetrahedral-cluster proves a powerful descriptive tool for $Mn_{10}Al_{29}$ diffraction intensities.

Reciprocal-space clusters composed of projected vertex-, edge-, polygon, and cell-centered 600-cells have a significant advantage over the real-space cluster descriptions more tra-

Table 4. Strongest (*hkl*) in $Mn_{10}Al_{29}$.

| (*h k l*) | $d_{hkl}$ [Å][a] | Multiplicity | Vertex–vertex (*k*-space-coord.) | Vertex–vertex (atom sites) | Intensity[b] |
|---|---|---|---|---|---|
| (0 6 0) | 2.07[c] | 2 | (0 3 0)–(0 $\bar{3}$ 0) | *CE–CE* | 100.0 |
| (7 0 2) | 2.01 | 4 | (2 0 5)–($\bar{5}$ 0 3) | *PG–PG* | 67.8 |
| | | | (5 5 $\bar{3}$)–($\bar{2}$ 5 $\bar{5}$) | *PPr–PPr* | |
| (4 0 5) | 2.07 | 4 | (6 0 0)–(2 0 $\bar{5}$) | *PG–PG* | 57.7 |
| | | | ($\bar{2}$ 5 5)–($\bar{6}$ 5 0) | *PPr–PPr* | |
| (2 3 5) | 2.06 | 8 | (2 0 5)–(0 $\bar{3}$ 0) | *PG–CE* | 54.8 |
| (5 3 3) | 2.09 | 8 | (0 3 0)–($\bar{5}$ 0 $\bar{3}$) | *CE–PG* | 53.3 |
| (6 3 0) | 2.12 | 4 | (6 0 0)–(0 $\bar{3}$ 0) | *PG–CE* | 52.1 |
| (0 0 10) | 1.25[d] | 2 | (2 0 5)–(2 0 $\bar{5}$) | *PG–PG* | 51.0 |
| (0 0 6) | 2.09 | 2 | ($\bar{5}$ 0 3)–($\bar{5}$ 0 $\bar{3}$) | *PG–PG* | 48.3 |
| | | | (5 5 3)–(5 5 $\bar{3}$) | *PPr–PPr* | |
| (7 0 8) | 1.26 | 4 | (2 0 5)–($\bar{5}$ 0 $\bar{3}$) | *PG–PG* | 47.7 |
| (4 5 0) | 2.06 | 4 | (2 0 $\bar{5}$)–($\bar{2}$ 5 $\bar{5}$) | *PG–PPr* | 46.8 |
| (3 5 2) | 2.09 | 8 | (5 5 $\bar{3}$)–(2 0 $\bar{5}$) | *PPr–PG* | 41.5 |
| (11 0 3) | 1.28 | 8 | (6 0 0)–($\bar{5}$ 0 $\bar{3}$) | *PG–PG* | 36.2 |
| (1 5 3) | 2.11 | 8 | (6 0 0)–(5 $\bar{5}$ $\bar{3}$) | *PG–PPr* | 32.7 |
| (2 2 5) | 2.22 | 2 | (0 $\bar{3}$ 0)–($\bar{2}$ $\bar{5}$ $\bar{5}$) | *CE–PPr* | 29.7 |
| (10 5 0) | 1.27 | 4 | (5 5 $\bar{3}$)–($\bar{5}$ 0 $\bar{3}$) | *PPr–PG* | 29.4 |
| (0 10 0) | 1.24 | 2 | ($\bar{6}$ 5 0)–($\bar{6}$ $\bar{5}$ 0) | *PPr–PPr* | 29.3 |
| (3 5 8) | 1.28 | 8 | (5 5 3)–(2 0 $\bar{5}$) | *PPr–PG* | 27.1 |
| (8 5 5) | 1.28 | 8 | (6 0 0)–($\bar{2}$ $\bar{5}$ $\bar{5}$) | *PG–PPr* | 25.0 |
| (5 2 3) | 2.25 | 8 | (5 5 3)–(0 3 0) | *PPr–CE* | 23.2 |
| (6 2 0) | 2.30 | 4 | (0 $\bar{3}$ 0)–($\bar{6}$ $\bar{5}$ 0) | *CE–PPr* | 21.3 |
| (2 8 5) | 1.30 | 8 | (0 3 0)–($\bar{2}$ $\bar{5}$ $\bar{5}$) | *CE–PPr* | 21.1 |
| (6 8 0) | 1.32 | 4 | (0 3 0)–($\bar{6}$ $\bar{5}$ 0) | *CE–PPr* | 12.2 |
| (2 0 6) | 2.01 | 8 | | – | 10.1 |
| (0 2 0) | 6.22 | 8 | | – | 9.8 |

[a] Table includes $d_{hkl}$ of up to 1.14 Å, corresponding to $Cu_{K\alpha 1}$ $2\theta$ of 85°. [b] As in Table 1 intensity is given per reflection, with neither atomic Debye–Waller nor Lorentz-polarization factors included. [c] Inner shell edges have $d_{hkl}$ ranging from 2.0 to 2.3 Å. [d] Inner shell second nearest neighbors have $d_{hkl}$ ranging from 1.2 to 1.35 Å.

ditionally used.[45,77–82] Real-space clusters have a fundamental ambiguity to them: they can be centered with equal validity around any of a number of different real space locations.[79] For example, in cell-centered structures, in one real space cluster description a site could be described as a cuboctahedron, but with another center of equally high symmetry, this same site would be a truncated tetrahedron.

By definition, reciprocal-space clusters can only be centered around one point, the reciprocal-space origin. In describing the strongest diffraction reflections, only a single reciprocal-space cluster is possible. In our real space hunt for metal crystals with projected 600-cell pseudosymmetries, especially when we turned to large unit cell examples, the real-space clusters could seem almost capriciously chosen. Reciprocal-space clusters remove such uncertainty. The crystals in this paper have a variety of complex real-space structures, but their reciprocal-space diffraction patterns all belong to one of four types: they are vertex-, edge-, polygon-, and cell-centered projections of the same 600-cell reciprocal-space cluster.

**Introduction to the Jones model**: That in tetrahedral crystals the strongest diffraction reflections are all pseudosymmetrically equivalent to one another is significant to their crystalline stability. The connection between strong diffraction peaks and metallic stability is probably easiest understood within the context of the venerable Jones model of metallic stability. This section is devoted to a brief introduction of this model couched in the LCAO language most familiar to the chemistry community.[28]

The Jones model is traditionally presented as a nearly-free electron model. Kinetic energy and spherical shells of electrons with similar kinetic energy certainly play a fundamental role in the theory. The Jones model speaks clearest to Hume-Rothery phases,[24,83–87] intermetallic structures with one to two valence electrons per atom, $e^-/a$. The reason why the Jones model is particularly suited for such compounds, however, is best understood within tight-binding electron theories such as an extended Hückel theory.[26–28,88,89]

We consider here three introductory cases: a linear chain, a square lattice, and an fcc structure.[24,27,90] Neither of the first two cases has much to do with actual Hume-Rothery metal structures; they are chosen instead to show us the constructs of Jones theory. In all three cases, we choose lattice constants of $a$ and hypothetical structures composed of a single Group 10–12 element. The linear chain will allow us to understand how orbital mixing takes place within the theory. The square lattice will allow us to understand that the Jones model provides concrete lower and upper theoretical bounds for the numbers of valence electrons per atom, $e^-/a$. The fcc structure, which is well known in Jones metal theory, will introduce newcomers to the multi-facetted Jones zone.

We consider first the 1D chain. As is traditional, we consider first purely free electrons. For such electrons, potential energy is zero, the total energy is solely the kinetic energy, and, as an electron's reciprocal space $k$ is proportional to the momentum, $E \propto k^2$. The total energy curve therefore has the shape of a parabola, shown in the first panel of Figure 29.

This free electron picture is amended by the incorporation of an actual crystal lattice, in this case a linear equally-spaced chain of Group 10–12 atoms with a lattice constant

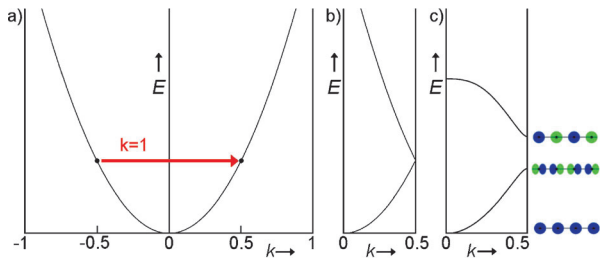


Figure 29. a) Linear chain free electron energy as a function of $k$, the crystal momentum; b) the "folded" format where $k$ vectors belonging to the same linear chain irreducible representation are placed in the same vertical column; and c) same energy bands in the presence of s and p orbital atoms. Band gap in c) at $k=0.5$ is caused by the difference in energy between the bonding p and the antibonding s orbitals. Note these $k=0.5$ orbitals both correspond to plane waves with wavelength $2a$ and are the result of the $k=1$ Jones-mixing indicated by the red horizontal arrow in panel a).

of $a$. Crystalline orbitals belonging to $k$ values differing from one another by whole integers can, in the presence of a crystal, mix with one another. (We use here the standard crystallographic nomenclature where ($hkl$) reflections are in whole numbers or, as in this case we are dealing with a 1D system reciprocal lattice, $k$ are single whole numbers.) We place those orbitals, which by crystalline symmetry are allowed to mix with one another, vertically atop one another: the parabola takes on the "folded" form shown in the second panel of Figure 29.

Orbitals generally perturb most orbitals with the same initial energy. The two states at $k=\frac{1}{2}$, being at the same initial energy, therefore perturb each other significantly. In the final panel of Figure 29 we show the perturbed wave functions at this $k$ value. From the perspective of $eH$ theory, the lower and higher energy orbitals are a bonding p state and an antibonding s state. Preparing for real crystal structures, the bonding p orbital will become HOMO-like and will be filled, while the antibonding s orbital will be LUMO-like and be unfilled. (In Group 10–12 tetrahedral structures, there are pseudo-bandgaps rather than actual bandgaps. Unlike what is found for the 1D chain, the language of HOMOs and LUMOs is therefore only approximate.)

Equally important are the two orbitals viewed from the nearly-free electron standpoint. From this perspective, we note that both the bonding p and antibonding s states resemble plane waves, plane waves with exactly the same wavelength, $\lambda=2a$, see Figure. Such a wavelength corresponds to $k=\pm\frac{1}{2}$. Within the context of free electrons, the bonding p and antibonding s states are linear combinations of the complex plane waves $e^{\frac{2\pi ikx}{a}}$ where $k=\pm\frac{1}{2}$.

Important in the Jones model are these initially free-electron plane wave orbitals which had to become mixed in order to form the linear chain $k=\pm\frac{1}{2}$ HOMO and LUMO orbitals. In the first panel of Figure 29 we indicate which points on the initial parabola correspond to these two plane waves. As this Figure shows, these two states differ from one another by $k=1$, represented in this Figure as an arrow.

In Jones theory, electron orbitals are perturbed free-electron orbitals. These perturbations are caused by the atoms in the crystal lattice. The magnitude of these perturbations is measured by the strength of individual diffraction peaks. In the 1D chain example, we recognize that $k=1$ is a strong diffraction peak. We therefore consider the bonding p state and an antibonding s states found at $k=\pm\frac{1}{2}$ to be the result of $k=1$ mixing between the $e^{\frac{2\pi i\frac{1}{2}x}{a}}$ and $e^{\frac{2\pi i\frac{-1}{2}x}{a}}$ plane waves. In Jones theory, the important orbital mixings are always consequences of strongly diffracting reciprocal lattice vectors.

We now consider the 2D square lattice. In Figure 30 we show the "spaghetti" diagram for the two lowest energy orbitals from Γ, ($hk$)=(0 0); to X, ($hk$)=($\frac{1}{2}$ 0); and finally M, ($hk$)=($\frac{1}{2}$ $\frac{1}{2}$). (We follow here crystallographic convention and do not place commas between the different vector terms.) As this Figure shows, at X the lower and higher energy orbitals are a very bonding p orbital and a net nonbonding s orbital, respectively, while at M the lower and higher energy orbitals are, respectively, a net-bonding p orbital and a very antibonding s orbital. All four orbitals are plane-wave-like. At X and M, as can be seen in the figure, their wavelengths are $\lambda=2a$ and $\lambda=\sqrt{2}a$, respectively.

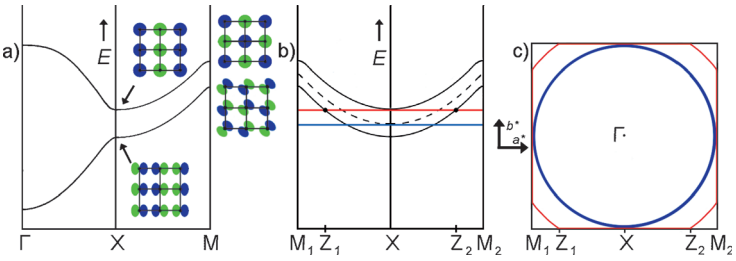


Figure 30. a) The two lowest energy square lattice s and p bands from Γ, (0 0); to X, ($\frac{1}{2}$ 0); to $M$, ($\frac{1}{2}\frac{1}{2}$). b) The energies of the two lowest bands from $M_1$, ($\frac{1}{2}\frac{1}{2}$); through X; to $M_2$, ($\frac{1}{2}\frac{1}{2}$). The separation between these two bands is due to Jones mixing. Band energies prior to mixing are shown as a dotted curve. c) The square lattice first Brillouin zone, shown as a black square. Inscribed inside this square is a blue circle. Both the blue circle in c) and the horizontal line in b) denote the same electron count. Optimal electron filling based on Jones mixing is shown in red. Both panels b) and c) indicate for this optimal electron count that, from $Z_1$ to $Z_2$, a single band is filled, while nearer $M_1$ and $M_2$, no orbital is filled. The black square, which is also termed the Jones zone,[24] and the blue circle therefore provide upper and lower bounds for the optimal filling shown in red.

Within the context of Jones theory, the splitting between bonding and non-bonding states at X is due to mixing between $e^{\frac{2\pi i\vec{k}\cdot\vec{x}}{a}}$ with $\vec{k}=(-\frac{1}{2}\ 0)$ and $\vec{k}=(\frac{1}{2}\ 0)$, the two states differing from one another by $\vec{k}=(1\ 0)$, a significant diffraction peak of the structure. In Jones theory, whenever two states are connected to one another by a strong diffraction peak, strong orbital mixing results. Thus the different energies of the bonding and antibonding states at M are the result of mixing between the $e^{\frac{2\pi i\vec{k}\cdot\vec{x}}{a}}$ for $\vec{k}=(-\frac{1}{2}\ -\frac{1}{2})$ and $\vec{k}=(\frac{1}{2}\ \frac{1}{2})$ states, two states differing from one another by $\vec{k}=(1\ 1)$, another strong diffraction peak.

In Figure 30 we show the first Brillouin zone for the 2D square lattice. This Brillouin zone is in the shape of a square. (1 0), the strong diffraction peak, connects one side of the first Brillouin zone to the opposite side. (1 0) being strong, not only can two X states couple, any state on one square-edge of the Brillouin zone with ($hk$) = ($\frac{1}{2}$ $k$) can couple to another state on the opposite side of the Brillouin zone with ($hk$) = ($-\frac{1}{2}$ $k$).

The first panel of Figure 30 shows the result of these mixings. Between X and M, the points under discussion here, there is a clear separation between lower and higher energy states. Within the context of Jones theory, this energy separation can be thought of as a splitting due to the intensity of the (1 0) diffraction peak.

We now consider estimates of the most stable electron count. We are interested here in developing bounds for the optimal electron count. The question we pose first is how to represent optimal electron counts on a spaghetti diagram. In the second panel of Figure 30 we enlarge the spaghetti diagram for ($h$ $k$) ranging from $M_1=(-\frac{1}{2}\ \frac{1}{2})$, to X = ($\frac{1}{2}$ 0), and finally to $M_2$ = ($\frac{1}{2}$ $\frac{1}{2}$). As this Figure shows, the two lowest

energy bands are both single-minimum curves, one cradled inside the other. Also placed in this figure, shown as a dotted line, is a third curve, the average of the previous two, which can be taken as the energies of these two bands before mixing had set in.

We focus first on this dotted line curve. The energy of this dotted line curve, unlike the other two, refers to energies where no Jones mixing has taken place. It describes purely free electrons. Were we to consider the purely free electron model and occupy all states up to the bottom-most point of the dotted line curve (this electron occupation is represented as a blue horizontal line), we would have an electron filling which corresponds in $k$ space to a circle just reaching the point X.

We now turn on Jones mixing. The dotted line curve splits into the two single minimum functions. We wish to fill as many as possible of the lower energy function while filling as few as possible of the higher energy function. The optimal electron filling is shown as a red horizontal line, which just touches the nadir of the higher energy curve. Were the electron filling to be any greater in value, we would begin filling the bottom of the upper curve, s states which are all slightly antibonding in character. Conversely were we to make the value any lower, we would depopulate states from the lower energy curve, p states which are all bonding in character.

As this Figure shows, the optimal electron count never intersects the upper energy curve composed solely of antibonding orbitals, and crosses the lower all-bonding curve at points $Z_1$ and $Z_2$. From $Z_1$ to X to $Z_2$, each point in k space has a single occupied orbital; from $M_1$ to $Z_1$ and $M_2$ to $Z_2$ there are no occupied orbital.

We now translate back these results to the Brillouin zone diagram. After Jones mixing has set in, all $\vec{k}$ at the edge of the Brillouin zone from $Z_1$ to X to $Z_2$ have a single filled orbital. Just as in the spaghetti diagram, those points on the zone edge closer to $M_1$ and $M_2$ are entirely devoid of electrons. Importantly, even at $X$ itself, the point where the upper energy function is lowest in energy, only a single one of the two lowest energy bands is filled. We represent this optimal filling by the red curve in the second panel of Figure 30. This red curve leaves the edges of the Brillouin zone exactly at the points $Z_1$ and $Z_2$. As at no point in the first Brillouin zone is any more than a single orbital filled, no point outside the Brillouin zone is ever filled.

The optimal filling being the one presented, establishing lower and upper bounds within the context of Jones theory becomes straightforward. A lower bound is the area of the largest possible circumscribed circle inside the Brillouin zone, represented as a blue circle (this blue circle corresponds to the blue horizontal line in the adjacent panel). An upper bound is the first Brillouin zone itself. In both these bounds just a single orbital is occupied. These areas may be initially thought of as being in units of orbitals per $k$-space unit cell. However, as we know that a reciprocal space unit cell corresponds to a given real space unit cell, and as we also know the number of atoms per real space unit cell, we can convert these answers from an orbital/reciprocal space unit cell area to an electron/atom basis. We explain the exact procedure in the following section.

We finally, briefly, turn to the 3D fcc structure. In 2D, the {1 0} diffraction peaks formed the *edges* of the first Brillouin zone. In the 3D fcc structure, the strong {2 0 0} and {1 1 1} reflections form the *faces* of a polyhedron, termed the Jones zone. This polyhedron is shown in Figure 31. Jones zones prove important in the qualitative understanding of noble metal tetrahedral structures.

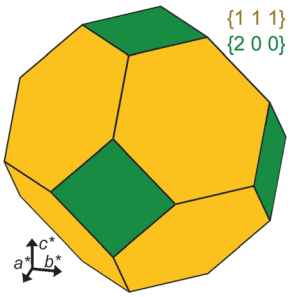


Figure 31. Face-centered-cubic Jones zone. The Jones zone is a truncated octahedron generated by the eight {1 1 1} and six {2 0 0} reflections.

**Group 10–12 tetrahedral-cluster structures**: The Jones model starts with the observation that free electrons with the same energy lie in $k$ space on a sphere centered at the origin and that crystal structures perturb these free electron states. Through the intermediary of the crystal structure, electronic states couple to one another. In the Jones model, electronic states connected to one another by $k$-space vectors, which are themselves strong diffraction vectors, are the electronic states which themselves couple the most strongly.

We therefore consider a $k$-space polyhedron whose faces are always connected to faces on the opposite side by strong diffracting reciprocal lattice vectors. These $k$-space polyhedra are termed Jones zones and represent those points in $k$ space whose electronic states most strongly couple with one another. From the perspective of Jones theory, a metal structure is most stable if its Jones zone is as similar as possible to the free electron sphere comprised of the metal's valence electrons.

Were the Jones zone and the free electron sphere to be identical, then orbitals at the Fermi energy, which in the free electron model are all states which lie on the *surface* of the free electron sphere, would also be points on the Jones zone and therefore would always be able to fully couple with one another. Orbitals at the Fermi energy would therefore split into lower energy, possibly bonding orbitals, and higher energy, possibly antibonding orbitals. In a metal, a pseudogap appears in its band diagram, reminiscent of a HOMO–LUMO gap in a molecule. Like a large HOMO–LUMO gap, a large pseudogap stabilizes the system.[24,91,92]

The Jones model presents clear lower and upper limits for the the number of valence electrons. The lower limit is de-

fined by the smallest free electron sphere which just touches a crystal structure's Jones zone.[93] The upper limit is the volume of the Jones zone itself expressed in units of valence electrons per atom, $e^-/a$.

When looking for an every day analogy of an ideal Jones zone, an excellent object to consider is a soccer-ball-shaped polyhedron, a polyhedron with 32 nearly equidistant faces which looks very much like a sphere. Tetrahedral metal structures can be viewed from this context. As we have seen, tetrahedral cluster structures can have even more than 32 strong diffraction peaks. Some have as many as 72. And these diffraction peaks are all pseudosymmetric with one another, have roughly the same $d_{hkl}$, and hence all lead to faces on the Jones zone all roughly equidistant from the center. A tetrahedral structure's Jones zone, could be even more sphere-like than a soccer ball polyhedron, and in one or two cases, their Jones zones actually are.

Tetrahedral-cluster structures can provide ideal Jones zone candidates. In this section we will consider this connection but only for compounds solely composed of Group 10–12 elements (though in order to find an example of an edge-centered tetrahedral cluster we will be forced to relax our criteria to a compound composed of Group 10 and 13 elements).

We restrict ourselves to elements from these three columns for mainly three reasons. First the Hume-Rothery electron phases can all be built up from the elements in the same three columns, and Hume-Rothery phases all obey specific electron count rules.[83–85,92,94] The very first successes for the Jones model included rationalizations of the specific electron count rules of noble-metal Hume-Rothery phases with the γ-brass and β-manganese crystal structures.[24] Second, no transition element with a partially filled *d*-band is included, so that we can assume a priori that the *d*-bands are entirely filled. And third, we include neither Groups 1 or 2 elements. Such elements are chemically so dissimilar to Group 11 and 12 elements, that assuredly factors other than just electron count must play a role in chemical stability.

We begin with a cubic structure, $Zn_{11}Au_{15}Cd_{23}$ (Figure 32), an $I_h$ quasicrystalline approximant structure which has the perhaps unique virtue that it is solely based on Groups 10–12 elements, see Appendix for experimental details.

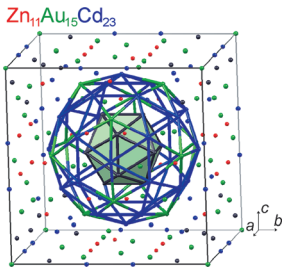


Figure 32. $Zn_{11}Au_{15}Cd_{23}$ unit cell. Elements are color-coded and a single vertex-centered cluster is shown. Inner and outer shells are represented, respectively, in filled-polyhedron and ball-and-stick formats. The polyhedral faces are green as an Au atom lies at the cluster center.

Although based on the Mackay real space cluster,[95] as Table 5, Figures 33 and 34 show, the diffraction in this crystal is well described by a reciprocal-space vertex-centered tetrahedral cluster. In Table 5 we list the strongest reflections for $Zn_{11}Au_{15}Cd_{23}$. The strongest diffraction peaks in this structure correspond to the nearest neighbors of a 13-atom reciprocal space cluster. This cluster is comprised of a site at the origin, *CC*, and twelve atoms in an icosahedron, *II*, centered on the origin at {5 0 3}. This cluster is shown in the left panel of Figure 34.

Table 5. Strongest (*hkl*) for $Zn_{11}Au_{15}Cd_{23}$.

| (*h k l*) | $d_{hkl}$ [Å][a] | Multiplicity | Vertex–vertex (*k*-space-coord.) | Vertex–vertex (atom sites) | Intensity[b] |
|---|---|---|---|---|---|
| (6 0 0) | 2.31 | 6 | (3 5 0)–($\bar{3}$ 5 0) | *II–II* | 100.0 |
| (5 3 2) | 2.25 | 24 | (5 0 $\bar{3}$)–(0 $\bar{3}$ $\bar{5}$) | *II–II* | 69.0 |
| (5 0 3) | 2.37 | 12 | (5 0 3)–(0 0 0) | *II–CC* | 36.8 |
| (6 2 0) | 2.19 | 12 | – | – | 24.1 |
| (4 3 3) | 2.37 | 6 | – | – | 14.5 |

[a] Table includes $d_{hkl}$ of up to 1.81 Å, corresponding to $Cu_{K\alpha 1}$ $2\theta$ of 50°. [b] Intensity as in Table 1 is given per reflection, with neither atomic Debye–Waller nor Lorentz-polarization factors included.

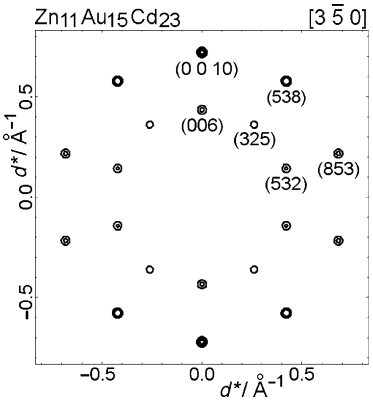


Figure 33. Diffraction pattern for a cluster-centered 3.1 nm diameter spherical crystallite of the vertex-centered $Zn_{11}Au_{15}Cd_{23}$ unit cell structure shown along the [3 5 0] direction. Only peaks whose peak height are $\geq$0.27 times the most intense peaks are shown.

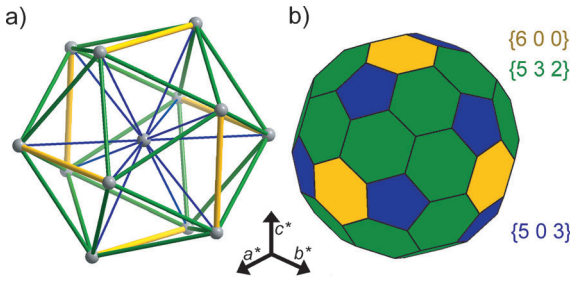


Figure 34. Vertex-centered reciprocal-space cluster and Jones zone for $Zn_{11}Au_{15}Cd_{23}$. The axes shown in the graph indicate relative directions only of the three reciprocal cell axes. $Zn_{11}Au_{15}Cd_{23}$ is a 1:1 quasicrystalline approximant. Its Jones zone differs significantly from the Jones zone presented previously for the 1:1 quasicrystalline approximant $Zn_{20}Al_{40}Mg_{40}$, see footnote in text. Cluster and Jones zone are not to scale of one another.

The reciprocal space tetrahedral cluster provides us with all the information required to make the Jones zone. We need to make a polyhedron where parallel faces on opposite sides of the polyhedron are related to one another by one of the edges of the reciprocal space tetrahedral cluster. In the right panel of Figure 34 we illustrate this Jones zone. The {6 0 0} edges, which are illustrated in yellow in this figure, generate six faces, shown in yellow in the Jones zone. Only three of these faces can be shown in our single hemisphere picture of the Jones zone. The other three faces are on the exact opposite side of the three shown faces and are thus connected to one another by vectors corresponding to the {6 0 0} edges of the reciprocal space tetrahedral cluster.

The reciprocal lattice cluster contains 42 distinct edges with near $I_h$ symmetry. The corresponding Jones zone is therefore a polyhedron of 42 facets with the same near $I_h$ symmetry. Its near spherical shape is self-evident and corresponds to the shape of the $C_{80}$ buckyball. It is even more spherical in shape than the $C_{60}$ shape, the latter shape being the shape which corresponds to soccer balls. The 1:1 quasicrystalline approximant $Zn_{11}Au_{15}Cd_{23}$ Jones zone reported here differs significantly from the Jones zone presented previously for the 1:1 quasicrystalline approximant $Zn_{20}Al_{40}Mg_{40}$.[96] The previously reported Jones zone is comprised of the {7 1 0}, {5 4 3}, and {5 5 0} reflections, with respective diffraction intensities of 23.0, 26.1, and 3.0%. Interestingly, the strongest intensity reflections for $Zn_{20}Al_{40}Mg_{40}$ are the {5 0 3}, {6 0 0}, and {5 3 2} reflections, with respective intensities of 100.0, 86.2, and 68.9%, the same three sets of reflections found in $Zn_{11}Au_{15}Cd_{23}$. In both structures the latter three reflections are the strongest, the second strongest, and the third strongest of all diffraction peaks up to $Cu_{K\alpha 1}$ of 50°. Previous work has suggested that the Jones mechanism for MacKay-based 1:1 quasicrystalline approximants takes place across {*hkl*} reflections where $h^2+k^2+l^2 = 50$.[96] Planes such as {7 1 0}, {5 4 3}, and {5 5 0} fufill this requirement. Were we to use these planes for $Zn_{11}Au_{15}Cd_{23}$, we would obtain lower and upper $e^-$bounds of 2.54–2.70 $e^-$/a, one whole electron/atom higher than the experimentally observed value. As $Zn_{20}Al_{40}Mg_{40}$, contains 40% of the group 2 element magnesium, a modified electron counting approach beyond that done in classic Hume-Rothery theory might be appropriate.[97]

Of the three sets of reciprocal lattice vectors used in making this Jones zone, that which has the smallest *d*-spacing is the {5 0 3} reflections. They therefore define the Jones model lower bound at an electron count of 1.42 $e^-$/a. This lower bound is computed from the volume of the corresponding free-electron sphere. The {5 0 3} peaks lead to a sphere with a radius of $\frac{\pi}{a}\sqrt{5^2+0^2+3^2} = 1.323$ Å$^{-1}$, where $a=$ 13.84 Å, the cell parameter. A sphere with this radius has volume 9.700 Å$^{-3}$. This number must be contrasted with the volume of a reciprocal space unit cell itself, $(\frac{2\pi}{a})^3 = 9.350\times 10^{-2}$ Å$^{-3}$. We conclude that the {5 0 3} sphere contains 103.8 reciprocal space unit cells ($103.8 = 9.700/9.350\times 10^{-2}$). In the free electron model reciprocal space unit cells equal orbitals/unit cell. The lower bound is therefore 103.8 orbitals per unit cell.

The upper bound is the volume of the Jones cell. In this case, the Jones cell has three face types ({5 0 3}, {6 0 0}, and {5 3 2}), planes which are at distances of 1.323, 1.362, and 1.399 Å$^{-1}$ from the origin. Numerical integration results in a volume of 11.548 Å$^{-3}$, equivalent to 123.5 orbitals per unit cell ($123.5 = 11.548/9.350\times 10^{-2}$).

As there are 146 atoms in each unit cell, and assuming two electrons fill each orbital, we deduce that $Zn_{11}Au_{15}Cd_{23}$ has lower and upper bounds of, respectively, 1.42 valence electrons/atom ($e^-$/a) ($1.42 = (103.8\times 2)/146$) and 1.69 $e^-$/a ($1.69 = (123.5\times 2)/146$). These numbers are tabulated in Table 6.

Of these two bounds, the upper bound proves more relevant. Within experimental error, it is the same as the experimentally determined electron count, which is calculated to be 1.69 $e^-$/a, ($1.69 = [(2\times 11)+(1\times 15)+(2\times 23)]/(11+15+23)$). In the limit of a perfectly spherical shape, or alternatively in the presence of very strong Jones orbital mixing, the upper bound of the Jones model becomes the

Table 6. Valence electron count for Group 10–12 tetrahedral cluster crystal structures.

| Compound | Vertices tetrahedral cluster | Number of faces | Cut-off[a] | Lower bound $e^-$/a | Range exptl. $e^-$/a | Upper bound $e^-$/a |
|---|---|---|---|---|---|---|
| | | vertex-centered cluster | | | | |
| $Zn_{11}Au_{15}Cd_{23}$ | *CC* + *II* | 42 | 0.30 | 1.42 | 1.69 | 1.69 |
| | | edge-centered cluster | | | | |
| $Pd_3Al_7$ | *CE* + *PG* | 32 | 0.30 | 1.83 | 2.10 | 2.38 |
| $Pd_3Al_7$[b] | *CE* + *PG* + *PPr* | 72 | 0.20 | 1.71 | 2.10 | 2.06 |
| | | polygon-centered cluster | | | | |
| $CdCu_2$ | *ITr* + *IL* + *IPr* | 18 | 0.30 | 0.97 | 1.33 | 1.40 |
| $Cu_3Cd_{10}$ | *ITr* + *IL* + *IPr* | 56 | 0.30 | 1.59 | 1.77[c] | 1.85 |
| | | cell-centered cluster | | | | |
| $Cd_3Cu_4$ | *IT* + *OT* + *OH* | 68 | 0.30 or 0.20 | 1.35 | 1.43 | 1.52 |
| $Cu_5Cd_8$[d] | *IT* + *OT* | 36 | 0.30 | 1.54 | 1.57–1.66 | 1.73 |
| $Cu_5Cd_8$ | *IT* + *OT* + *OH* | 36 | 0.20 | 1.54 | 1.57–1.66 | 1.73 |
| $Pt_5Zn_{21}$ | *IT* + *OT* | 36 | 0.30 or 0.20 | 1.54 | 1.62 | 1.73 |

Substitute a times sign for the x [a] Only {*hkl*} with intensities higher than stated cut-off × maximum intensity reflection are considered in Jones calculation. If a vertex causes a single (*hkl*) to exceed a given cut-off all reflections due to the vertex type are included. [b] The $Pd_3Al_7$ single crystal refinement lists variations in thermal parameters from $B = 0.02$ to 1.97. The lower/upper bounds and the experimental $e^-$/a are therefore only approximately known. [c] The $Cu_3Cd_{10}$ phase has variable composition. However, as there is considerable vacancy disorder, we can calculate the Jones volume only where there is a solved single crystal structure. In this solved structure there are 26.4 atoms/unit cell. [d] $Cu_5Cd_8$ is a γ-brass structure. Its range of experimental electron counts resembles that of many other γ-brass structures. In the case of $Cu_5Cd$ there is substitutional, but no vacancy, disorder. Therefore the upper bound Jones estimate stays at a constant value.

actual predicted Jones model electron count. It is plausible that up to three significant figures in its electron count, $Zn_{11}Au_{15}Cd_{23}$ has reached this limit.

In Table 7 we list the strongest reflections for the cell-centered $Pt_5Zn_{21}$ structure. As expected, its strong diffraction peaks can be rationalized based on a reciprocal lattice cell-centered tetrahedral cluster with *IT*, *OT* and *OH* sites at, respectively, {3 3 3}, {$\bar{5}$ $\bar{5}$ $\bar{5}$} and {10 0 0}. As this table shows, the most central edges, *IT–IT* (the {6 6 0} reflections) and *IT–OT* (the {8 2 2} reflections) are the most significant of all diffraction peaks. However, the next most central edges, those which include the *OH* site (the {5 5 5} and {7 3 3} reflections), are the third and sixth strongest peaks overall. Their intensities, on a per edge basis, are, however, more than a factor of ten weaker than the *IT–IT* and *IT–OT* reflections.

This table introduces us to a short-coming in the traditional Jones zone model. Once included as a principal diffraction peak, the traditional Jones model does not further take into account relative intensities. While the {5 5 5} and {7 3 3} undoubtedly play a role in the phase stability of $Pt_5Zn_{21}$, their role should be less than the role played by the {6 6 0} and {8 2 2} reflections.

Table 7. Strongest (*hkl*) for $Pt_5Zn_{21}$.

| (*h k l*) | $d_{hkl}$ [Å][a] | Multiplicity | Vertex–vertex (*k*-space-coord.) | Vertex–vertex (atom sites) | Intensity[b] |
|---|---|---|---|---|---|
| (6 6 0) | 2.13 | 12 | (3 3 3)–($\bar{3}$ $\bar{3}$ 3) | *IT–IT* | 100.0 |
| (8 2 2) | 2.13 | 24 | (3 $\bar{3}$ $\bar{3}$)–($\bar{5}$ $\bar{5}$ $\bar{5}$) | *IT–OT* | 33.4 |
| (5 5 5) | 2.09 | 8 | (5 5 $\bar{5}$)–(0 0 $\overline{10}$) | *OT–OH* | 6.7 |
| | | | (5 $\bar{5}$ 5)–(0 $\overline{10}$ 0) | *OT–OH* | |
| | | | ($\bar{5}$ 5 5)–($\overline{10}$ 0 0) | *OT-OH* | |
| (4 2 2) | 3.69 | 24 | – | – | 4.9 |
| (3 3 3) | 3.48 | 8 | – | – | 4.1 |
| (7 3 3) | 2.21 | 24 | (10 0 0)–(3 $\bar{3}$ $\bar{3}$) | *IT–OH* | 3.6 |
| (5 1 1) | 3.48 | 24 | – | – | 3.4 |

[a] Table includes $d_{hkl}$ of up to 1.81 Å, $Cu_{K\alpha1}$ $2\theta$ of 50°. [b] Intensity as in Table 1 is given per reflection, with neither atomic Debye–Waller nor Lorentz-polarization factors included.

Within the confines of the traditional Jones model, we therefore only wish to consider the effect of the most significant peaks. Examining the structures reported in this paper, we see that a cut-off of reflections whose intensities are at least 30% generally provides a clean break between innermost shell and more exterior edges. As Table 6 shows, changing this cut-off from 0.30 to 0.20 does not in most cases substantially change the Jones model estimates.

That the Jones model requires an ad hoc cut-off value nevertheless is a potential liability to the model. Yes, the matching of experimental electron counts to upper and lower Jones bounds can be insensitive to the exact cut-off used. But with any arbitrary cut-off, the possibility that agreement between theory and experiment is being forced rather than being naturally achieved is always an issue.

Using this cut-off value, for $Pt_5Zn_{21}$ we include only the *IT–IT* or *IT–OT* reflections. These two edge types lead to the two Jones zone face types presented in Figure 35. The illustrated Jones zone is a well-known one,[24] it is that of γ-brass and consists of 36 faces with $O_h$ symmetry.

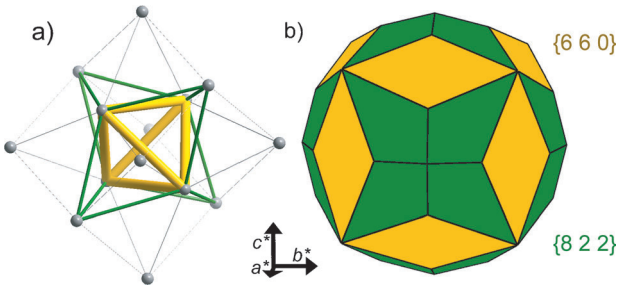


Figure 35. Cell-centered reciprocal-space cluster and Jones zone for $Pt_5Zn_{21}$. Colored cluster based on sites with reflection intensities ≥0.30 of the most intense reflection. Reflections are color-coded. The reflections are listed in descending order of intensity and cluster cylinder radii are proportional to intensity see Table 7. The axes shown in the graph indicate relative directions only of the three reciprocal cell axes. Cluster and Jones zone are not to scale of each other.

The Jones zone approaches a spherical symmetry, though not quite as spherical as the $Zn_{11}Au_{15}Cd_{23}$ Jones zone. Its volume is 360.0 orbitals per unit cell and, as there are 416 atoms in each unit cell, we deduce a Jones volume of 1.73 valence electrons/atom ($e^-$/a) for example, $1.73 = (360.0 \times 2)/416$. These values can be contrasted with the experimental value of 1.62 $e^-$/a, $1.62 = [(0 \times 5) + (2 \times 21)]/(5+21)$ and a lower bound of 1.54 $e^-$/a, see Table 6.

The edge-centered $Pd_3Al_7$ further illustrates the imprecision introduced into the Jones model by the choice of cut-off. As Table 8 illustrates, its diffraction pattern can be interpreted with an edge-centered reciprocal space cluster. The *CE* site is at {0 0 4}; *PG* at {8 3 0}, {$\bar{3}$ 5 0}, and {$\overline{10}$ 0 0};

Table 8. Strongest (*hkl*) in $Pd_3Al_7$.

| (*h k l*) | $d_{hkl}$ [Å][a] | Multiplicity | Vertex–vertex (*k*-space-coord.) | Vertex–vertex (atom sites) | Intensity[b] |
|---|---|---|---|---|---|
| (0 0 8) | 2.07 | 2 | (0 0 4)–(0 0 $\bar{4}$) | *CE–CE* | 100.0 |
| (8 3 4) | 2.06 | 8 | (8 3 0)–(0 0 $\bar{4}$) | *PG–CE* | 64.1 |
| (3 5 4) | 2.04 | 8 | (0 0 4)–($\bar{3}$ $\bar{5}$ 0) | *CE–PG* | 59.2 |
| (10 0 4) | 2.04 | 4 | (0 0 4)–($\overline{10}$ 0 0) | *CE-PG* | 55.7 |
| (11 2 0) | 2.01 | 4 | (8 $\bar{3}$ 0)–($\bar{3}$ $\bar{5}$ 0) | *PG–PG* | 53.3 |
| | | | (3 5 7)–($\bar{8}$ 3 7) | *PPr–PPr* | |
| (7 5 0) | 1.98 | 4 | ($\bar{3}$ 5 0)–($\overline{10}$ 0 0) | *PG–PG* | 48.9 |
| | | | (10 0 7)–(3 $\bar{5}$ 7) | *PPr-PPr* | |
| (0 6 0) | 2.05 | 2 | (8 3 0)–(8 $\bar{3}$ 0) | *PG–PG* | 49.4 |
| | | | ($\bar{8}$ 3 7)–($\bar{8}$ $\bar{3}$ 7) | *PPr–PPr* | |
| (5 2 7) | 2.00 | 8 | (8 $\bar{3}$ 0)–(3 $\bar{5}$ $\bar{7}$) | *PG–PPr* | 22.6 |
| (2 3 7) | 2.02 | 8 | ($\bar{8}$ 3 7)–($\overline{10}$ 0 0) | *PPr–PG* | 22.2 |
| (6 0 7) | 2.02 | 4 | (3 $\bar{5}$ 7)–($\bar{3}$ $\bar{5}$ 0) | *PPr–PG* | 21.1 |
| (5 2 1) | 3.63 | 8 | | – | 18.3 |
| (3 1 4)[c] | 3.51 | 8 | | – | 16.6 |
| (3 5 3) | 2.16 | 8 | (3 5 7)–(0 0 4) | *PPr–CE* | 12.8 |
| (8 3 3) | 2.19 | 8 | (0 0 $\bar{4}$)–($\bar{8}$ $\bar{3}$ $\bar{7}$) | *CE–PPr* | 11.5 |
| (10 0 3) | 2.15 | 4 | (10 0 7)–(0 0 4) | *PPr–CE* | 12.2 |

[a] Table includes $d_{hkl}$ of up to 1.81 Å, corresponding to $Cu_{K\alpha1}$ $2\theta$ of 50°. [b] As in Table 1 intensity is given per reflection, with neither atomic Debye–Waller nor Lorentz-polarization factors included. [c] Nine more reflections with $d_{hkl}$ ranging from 3.1 to 3.8 have intensities between those observed for {3 1 4} and {10 0 3}, that is, have intensities greater or equal to the weakest inner shell reflections *CE–PPr* set of reflections.

and *PPr* at {10 0 7}, {3 5 7}, and {$\bar{8}$ 3 7}. As Table 8 shows, edges involving solely *CE* and *PG* range in intensity from 50-100% in intensity; edges where one of the two sites is *PPr* range from 10–20% in intensity.

Figure 36 graphically illustrates that the inner-most edges are strongest and diffraction reflections become weaker as their corresponding edge becomes less central. It is here where the imprecision of the Jones model becomes apparent. While *CE–PPr* and *PG–PPr* edges are at least a factor of two weaker than the *PG–PG* edges, they are not so weak that they should be entirely ignored. In Table 6, we contrast two Jones zones. In the first, only reflections based on *CE* and *PG* sites are included; in the second, sites involving *PPr* are added to the mix. This corresponds to cut-offs of 0.30 and 0.20, respectively.

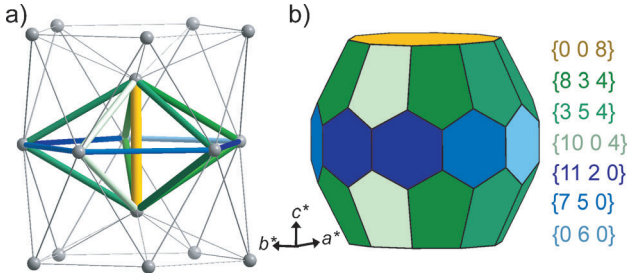


Figure 36. Edge-centered reciprocal-space cluster and Jones zone for $Pd_3Al_7$. Colored cluster based on sites with reflection intensities $\geq$0.30 of the most intense reflection. Reflections are color-coded. The reflections are listed in descending order of intensity and cluster cylinder radii are proportional to intensitys, see Table 8. The axes shown in the graph indicate relative directions only of the three reciprocal cell axes. Cluster and Jones zone are not to scale of each other.

The Jones model upper bound changes from 2.38 to 2.06 $e^-$/a. Lower bounds also change significantly from 1.83 to 1.71 $e^-$/a. Lower and upper bounds differ from one another by as much as 0.55 $e^-$/a, 0.55 = 2.38–1.83; this large spread can be attributed to the less spherical nature of the Jones zone. Given the large spread, it is not surprising that the actual electron count is found between the two bounds: this actual electron count is 2.1 $e^-$/a.

To us, the primary issue is not whether the 0.30 or 0.20 cut-off is more accurate (though in this paper we adopt a cut-off of 0.30), the issue is that a cut-off needs to be chosen at all. All tetrahedral edges are pseudosymmetric with one another, if one edge stabilizes the structure, they all must stabilize the system. Cutting off weaker reflections due to the all-or-nothing nature of the Jones zone results in the loss of significant attributes of the electronic structure.

In all three cases discussed so far, there is good agreement between the lower and upper bounds of the Jones model and observed electron counts. This agreement suggests that the Jones model can be used to account for phase stability in Group 10–12 tetrahedral cluster structures in general. In this light, compounds based on copper and cadmium prove of genuine interest. The phase diagrams for this pair of elements is shown in Figure 37.[98] Four Cu–Cd phases are known, in ascending concentration of cadmium they are $CdCu_2$, $Cd_3Cu_4$, $Cu_5Cd_8$, and $Cu_3Cd_{10}$.

The first and the fourth in this list of structures have polygon-centered tetrahedral cluster structures. The remaining two are cell-centered. Remarkably, for these two elements, and, to our knowledge only for these two elements, all known binary phases are different variants of tetrahedral cluster crystal structures. Tables 9–11 list the principal reflections for the three structures, $CdCu_2$, $Cu_5Cd_8$, and $Cu_3Cd_{10}$, Table 2 having previously listed the principal $Cd_3Cu_4$ reflections.

$CdCu_2$ presents us with the second main limitation inherent in the Jones model. $CdCu_2$, which crystallizes in the hexagonal $MgZn_2$ structure, has diffraction spots which can be understood in reference to a polygon-centered cluster with *ITr*, *IL*, *IPr*, and *OPr* sites located at, respectively, {0 1 0}, {0 0 3}, {2 0 2}, and {2 $-\bar{2}$ 3}. The issue here is not the cut-off value. Reflections involving *ITr*, *IL* and *IPr* sites are at least a factor of three stronger than sites involving the *OPr* site. The cut-off at 0.30 is therefore clean: edges involving *ITr*, *IL*, and *IPr* edges should be included while those involving *OPr* should not. The issue lies in the $d_{hkl}$.

While the edges in the reciprocal space cluster are all pseudosymmetric with one another and before projection were of equal length, perhaps due to the small size of the $CdCu_2$ structure and the concomitant rounding to whole number diffraction lattice vectors, their final observed $d_{hkl}$

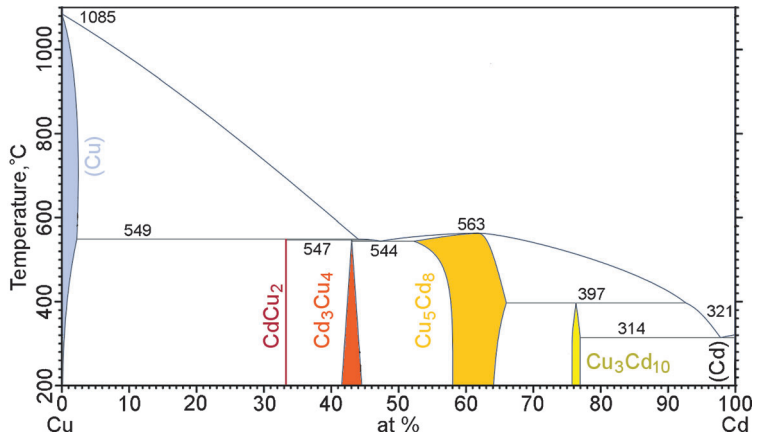


Figure 37. Cu–Cd binary phase diagram adapted from Massalski.[98] The four known stable Cu–Cd phases are color-coded, ox-blood $CdCu_2$; carnelian: $Cd_3Cu_4$; Spanish yellow: $Cu_5Cd_8$; and fluorescent chartreuse: $Cu_3Cd_{10}$. See Figure 42.

Table 9. Strongest (*hkl*) for $CdCu_2$.

| (*h k l*) | $d_{hkl}$ [Å][a] | Multiplicity | Vertex–vertex (*k*-space-coord.) | Vertex–vertex (atom sites) | Intensity[b] |
|---|---|---|---|---|---|
| (1 1 2) | 2.11 | 12 | (1 $\bar{1}$ 0)–(0 $\bar{2}$ $\bar{2}$) | *ITr–IPr* | 100.0 |
| | | | (2 0 2)–($\bar{1}$1 0) | *IPr–ITr* | |
| (1 1 0) | 2.48 | 6 | (0 1 0)–($\bar{1}$ 0 0) | *ITr–ITr* | 77.2 |
| (0 0 4) | 2.00 | 2 | (2 0 2)–(2 0 $\bar{2}$) | *IPr–IPr* | 75.8 |
| | | | (0 $\bar{2}$ 2)–(0 $\bar{2}$ $\bar{2}$) | *IPr–IPr* | |
| | | | ($\bar{2}$ 2 2)–($\bar{2}$ 2 $\bar{2}$) | *IPr–IPr* | |
| (1 0 3) | 2.26 | 12 | (0 0 3)–($\bar{1}$ 0 0) | *IL–ITr* | 75.2 |
| | | | ($\bar{1}$ 0 0)–($\bar{2}$ 0 $\bar{3}$) | *ITr–OPr* | |
| (2 0 1) | 2.07 | 12 | (2 0 2)–(0 0 $\bar{3}$) | *IPr–IL* | 71.3 |
| (2 0 0) | 2.15 | 6 | (0 0 3)–($\bar{2}$ 0 3) | *IL–OPr* | 25.7 |
| | | | (0 0 $\bar{3}$)–($\bar{2}$ 0 $\bar{3}$) | *IL–OPr* | |
| (2 0 2) | 1.89 | 12 | – | – | 7.7 |
| (1 0 2) | 2.93 | 12 | – | – | 4.0 |

[a] Table includes $d_{hkl}$ of up to 1.81 Å, corresponding to $Cu_{K\alpha1}$ $2\theta$ of 50°. [b] Intensity as in Table 1is given per reflection, with neither atomic Debye-Waller nor Lorentz-polarization factors included.

Table 10. Strongest (*hkl*) for $Cu_5Cd_8$.

| (*h k l*) | $d_{hkl}$ [Å][a] | Multiplicity | Vertex–vertex (*k*-space-coord.) | Vertex–vertex (atom sites) | Intensity[b] |
|---|---|---|---|---|---|
| (3 3 0) | 2.26 | 12 | ($\frac{3}{2}$ $\frac{3}{2}$ $\frac{3}{2}$)–($\frac{3}{2}$ $\frac{3}{2}$ $\frac{3}{2}$) | *IT–IT* | 100.0 |
| (4 1 1) | 2.26 | 24 | ($\frac{3}{2}$ $\frac{3}{2}$ $\frac{3}{2}$)–($\frac{5}{2}$ $\frac{5}{2}$ $\frac{5}{2}$) | *IT–OT* | 65.0 |
| (3 3 2) | 2.04 | 8 | ($\frac{5}{2}$ $\frac{5}{2}$ $\frac{5}{2}$)–(0 0 $\bar{5}$) | *OT–OH* | 22.8 |
| | | | ($\frac{5}{2}$ $\frac{5}{2}$ $\frac{5}{2}$)–(0 $\bar{5}$ 0) | *OT–OH* | |
| | | | ($\frac{5}{2}$ $\frac{5}{2}$ $\frac{5}{2}$)–($\bar{5}$ 0 0) | *OT–OH* | |
| (4 2 2) | 1.96 | 24 | (5 0 0)–($\frac{3}{2}$ $\frac{3}{2}$ $\frac{3}{2}$) | *IT–OH* | 17.1 |
| (1 1 0) | 6.78 | 24 | – | – | 16.1 |
| (5 1 0) | 3.48 | 24 | – | – | 12.5 |

[a] Table includes $d_{hkl}$ of up to 1.81 Å, $Cu_{K\alpha1}$ of 50°. [b] Intensity as in Table 1 is given per reflection, with neither atomic Debye-Waller nor Lorentz-polarization factors included.

Table 11. Strongest (*hkl*) for $Cd_3Cu_{10}$.

| (*h k l*) | $d_{hkl}$ [Å][a] | Multiplicity | Vertex–vertex (*k*-space-coord.) | Vertex–vertex (atom sites) | Intensity[b] |
|---|---|---|---|---|---|
| (0 0 4) | 2.19 | 2 | (3 0 2)–(3 0 $\bar{2}$) | *IPr–IPr* | 100.0 |
| | | | ($\bar{3}$ 3 2)–($\bar{3}$ 3 $\bar{2}$) | *IPr–IPr* | |
| | | | (0 $\bar{3}$ 2)–(0 $\bar{3}$ $\bar{2}$) | *IPr–IPr* | |
| (3 0 1) | 2.26 | 12 | (3 0 2)–(0 0 $\bar{3}$) | *IL–IPr* | 52.1 |
| | | | (3 $\bar{3}$ 3)–(0 $\bar{3}$ 2) | *OPr–IPr* | |
| | | | (0 3 3)–($\bar{3}$ 3 2) | *OPr–IPr* | |
| (2 1 2) | 2.27 | 24 | (2 $\bar{2}$ 0)–(0 $\bar{3}$ $\bar{2}$) | *ITr–IPr* | 50.4 |
| (2 0 3) | 2.24 | 12 | (0 0 3)–($\bar{2}$ 0 0) | *IL–ITr* | 36.8 |
| (2 2 0) | 2.03 | 6 | (0 2 0)–($\bar{2}$ 0 0) | *ITr–ITr* | 36.1 |
| (3 0 0) | 2.34 | 6 | (0 0 3)–($\bar{3}$ 0 3) | *IL–OPr* | 22.1 |
| | | | (0 0 $\bar{3}$)–($\bar{3}$ 0 $\bar{3}$) | *IL–OPr* | |
| (1 0 3) | 2.69 | 12 | ($\bar{2}$ 0 0)–($\bar{3}$ 0 $\bar{3}$) | *ITr–OPr* | 20.6 |
| (2 1 0) | 2.66 | 12 | – | – | 16.3 |
| (2 0 2) | 2.74 | 12 | – | – | 16.2 |

[a] Table includes $d_{hkl}$ of up to 1.81 Å, corresponding to $Cu_{K\alpha1}$ $2\theta$ of 50°. [b] Intensity as in Table 1is given per reflection, with neither atomic Debye–Waller nor Lorentz-polarization factors included.

vary from 2.00 to 2.48 Å. As Table 9 and Figure 38 show, although there are five intense reflections ({1 1 2}, {1 1 0}, {0 0 4}, {1 0 3}, and {2 0 1} corresponding to *ITr–IPr*, *ITr–ITr*, *IPr–IPr*, *IPr–IL*, and *IL–IPr*), respectively; only two of these five reflections have a large enough $d_{hkl}$ to actually form faces in the Jones zone. The Jones zone does not incorporate the effect of three of the five principal reflections responsible for the $CdCu_2$ phase stability. Nonetheless, as Table 6 shows, the actual $CdCu_2$ electron count lies comfortably between the lower and upper Jones zone bounds.

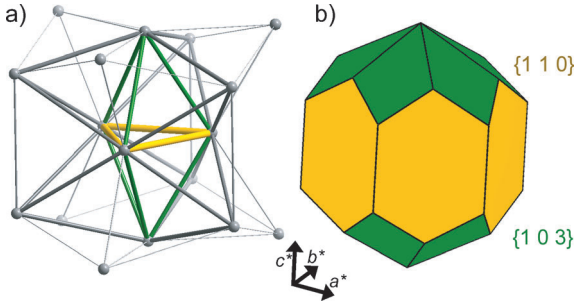


Figure 38. Polygon-centered reciprocal-space cluster and Jones zone for $CdCu_2$. Colored cluster based on sites with reflection intensities $\geq$0.30 of the most intense reflection. Only two of the five reflections which meet this criterion have large enough $d_{hkl}$ values to actually appear in the Jones zone. These two reflections are color-coded. The reflections are listed in descending order of intensity. Cluster cylinder radii are proportional to intensity. Reflections are color-coded, see Table 9. The axes shown in the graph indicate relative directions only of the three reciprocal cell axes. Cluster and Jones zone are not to scale of each other. The pictured Jones zone is the same shape as that reported for AgZn elsewhere.[25]

The next two phases in the Cu–Cd phase diagram are both based on cell-centered clusters. $Cu_5Cd_8$ is a γ-brass structure and our previous discussions on this structure and on the $Pt_5Zn_{21}$ γ-brass superstructure examine almost all the relevant issues. Its principal diffraction peaks, reciprocal lattice cluster, and Jones zone are shown in Table 10 and Figure 39.

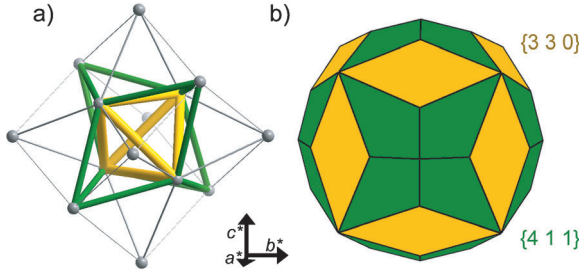


Figure 39. Cell-centered reciprocal-space cluster and Jones zone for $Cu_5Cd_8$. Cluster based on sites with reflection intensities $\geq$0.30 of the most intense reflection, see Figure 35 for a similar figure. The reflections are listed in descending order of intensity and cluster cylinder radii are proportional to intensity, see Table 10. The axes shown in the graph indicate relative directions only of the three reciprocal cell axes. Cluster and Jones zone are not to scale of each other.

One important distinction between $Cu_5Cd_8$ and $Pt_5Zn_{21}$, is that, due to rounding, both the *IT–OH* and *OT–OH* reflections have significantly shorter $d_{hkl}$ than the *IT–IT* and *IT–OT* peaks. It therefore proves irrelevant to the Jones zone, whether edges involving *OH* sites are included. A change in cut-off from 0.30 to 0.20 does lead to inclusion of edges involving *OH* sites, but no change in either Jones lower or upper bounds ensues from this change.

The $Cd_3Cu_4$ structure presents us with one last issue in our Jones model treatment. This structure, being comprised of cell-centered tetrahedral clusters, has as principal edges in descending order of importance *IT–IT*, *IT–OT*, and *IT–OH* and *OT–OH*, these last two reflections being roughly equal in importance (see Table 2). The issue is whether in evaluating the importance of a given Jones face intensities on a per reflection or a per edge basis should be considered. If a reflection has a strong intensity, then in the Jones model this should result in a strong mixing of states. From the perspective of the Jones model, it does not matter if a multitude of equivalent edges are responsible for the reflection intensity.

We therefore assume that in the choosing of Jones zone cut-off values, intensity on a per reflection basis should be used. For $Cd_3Cu_4$, the *OT–OH* reflection is only slightly weaker than the *IT–IT* and *IT–OT* reflections. With this understanding, edges involving the *OH* site are well above the 0.30 threshold and certainly require inclusion. In Figure 40, we therefore construct our Jones zone using all edges involving *IT*, *OT*, and *OH* sites. The inclusion of the *OH* sites leads to four rather than two faces in the Jones zone. The zone is reasonably spherical. Lower and upper bounds are 1.35 and 1.52 $e^-$/a compared to an experimental value of 1.43 $e^-$/a.

The final Cu–Cd phase is $Cu_3Cd_{10}$, a polygon-centered cluster structure. In this structure *ITr*, *IL*, *IPr*, and *OPr* sites are located at, respectively, {0 2 0}, {0 0 3}, {3 0 2}, and {3 $\bar{3}$ 3}. Its diffraction data are shown in Table 11. As this table shows, reflections based solely on *ITr*, *IL*, and *IPr* edges are two to four times stronger than those involving *OPr* sites. Using a cut-off of 0.30, only the former edges are included. The reciprocal space cluster and Jones zone are illustrated in Figure 41. The Jones zone is somewhat spherical with lower and upper bounds of 1.59 and 1.83 $e^-$/a, values which comfortably straddle the experimental electron count of 1.77 $e^-$/a.

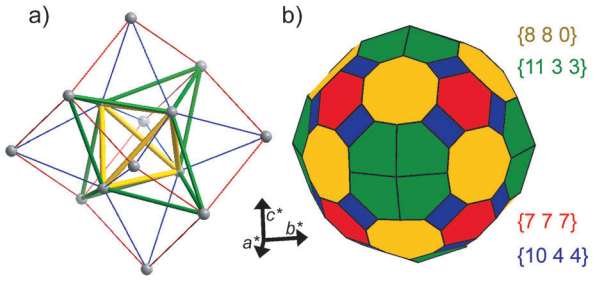


Figure 40. Cell-centered reciprocal-space cluster and Jones zone for $Cd_3Cu_4$. Colored cluster based on sites with reflection intensities $\geq$0.30 of the most intense reflection. Reflections are color-coded. The reflections are listed in descending order of intensity and cluster cylinder radii are proportional to intensity, see Table 2. The axes shown in the graph indicate relative directions only of the three reciprocal cell axes. Cluster and Jones zone are not to scale of each other.

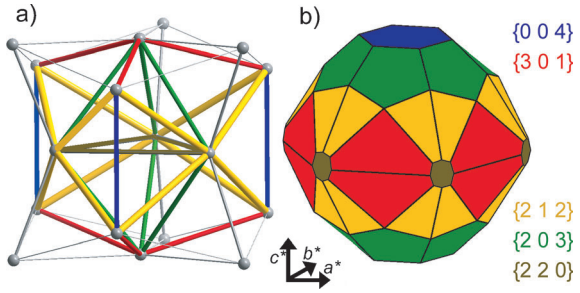


Figure 41. Polygon-centered reciprocal-space cluster and Jones zone for $Cu_3Cd_{10}$. Colored cluster based on sites with reflection intensities $\geq$0.30 of the most intense reflection. Reflections are color-coded. The reflections are listed in descending order of intensity and cluster cylinder radii are proportional to intensity, see Table 11. The axes shown in the graph indicate relative directions only of the three reciprocal cell axes. Cluster and Jones zone are not to scale of each other.

In all seven cases considered in this section, see Table 6, the Jones zone model provides reasonable lower and upper bounds for phase stability, this despite the inherent liabilities of the method. We leave this section with a graphical representation of the overall Jones model. In Figure 42 we illustrate the Jones zones for all four known Cu–Cd phases, using in all four of the zones identical $e^-$/a scales. Their Cd content ranges from 33–77 %. In going from the most Cd-poor to the most Cd-rich phase, that is, in progressing from $CdCu_2$, to $Cd_3Cu_4$, to $Cu_5Cd_8$, and finally to $Cu_3Cd_{10}$, their experimental $e^-$/a progress from 1.33 to 1.43 to 1.62 to 1.77, just as their Jones zone volumes travel from 1.40, to 1.52, to 1.73, and finally to 1.85 $e^-$/a.

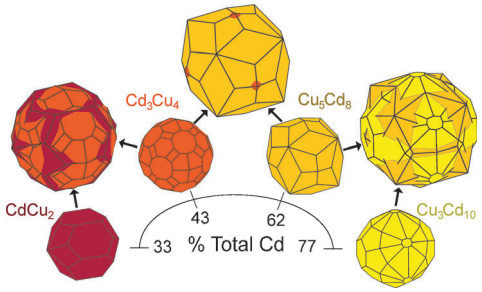


Figure 42. The Jones zones of the four binary Cu–Cd phases in order of ascending cadmiun content. Phases are color-coded in the color version of figure. Ox blood: $CdCu_2$; carnelian: $Cd_3Cu_4$; Spanish yellow: $Cu_5Cd_8$; and fluorescent chartreuse: $Cu_3Cd_{10}$. Single Jones zones are plotted at the same $e^-$/a scale. Neighboring Jones zones show the more cadmium-rich Jones zone enveloping the less cadmium-rich phase.

Each Jones zone volume is only slightly bigger than the next volume, but the four volumes track the actual number

of valence electrons in these structures. In Figure 42 we directly compare each Jones zone with the preceding zone, following the progression of the phases. Each zone partially swallows up the preceding zone. As the cadmium content increases, so does the number of valence electrons. Within the constraints of possible crystal structures, Jones zones recapitulate free electron spheres.

**Symmetry and electrons**: This paper is long. The basic story it tells has been told before. Electronic states mix and stabilize the structure. Symmetry organizes the way this mixing occurs. The twist here is that the symmetry comes from two different sources. On the one hand there is the crystal, on the other hand there are the electrons. The crystal symmetry is described by a space group; the electron symmetry, at first, is that of a free electron sphere. We can couch both symmetries in terms of reciprocal space. Orbital mixing proves best when the crystal symmetry, best thought of in terms of the Jones zone, mimics the second.

The crux of the paper is that were it possible for the crystal to go beyond the most symmetrical 3D point groups, $O_h$ and $I_h$, and thus have even greater numbers of faces in their Jones zone, it would be possible to have even more mixing on the Fermi surface free electron sphere. Amazingly, crystals find a way to do so. They cannot find more 3D symmetries; there are none: they find 3D pseudosymmetries instead. Knowing best the language of perfect symmetry, we invoke a 4D Platonic solid to describe them.

Tetrahedrally packed quasicrystalline approximants and Frank–Kasper phases crystals whose highest symmetry sites are $T_d$, $T_h$, $D_{3h}$,, or $C_{2v}$, adopt a collection of true and pseudosymmetry axes which are all projections of objects with the same 4D point-group. And this point group organizes the faces of their nearly sphere-like Jones polyhedra into pseudosymmetrically equivalent faces. Mixing, pseudogaps, and stability ensue. It's a bit of a mouthful, but it is just symmetry controlling the fate of electronic states and electronic states controlling the stability of molecules.

**Mysterious metals**: Hydrogen and oxygen form $H_2O$; the stoichiometry and the number of bonds correspond to the hydrogen and oxygen valencies. Metals do not work the same way. Their stoichiometry, the number of their bonds, and their atomic valencies seem to cascade to more and more complex formulations. It seems hopeless to explain in any language as straightforward as that used for hydrogen and oxygen, why copper and cadmium make four compounds with the stoichiometries $CdCu_2$, $Cd_3Cu_4$, $Cu_5Cd_8$, and $Cu_3Cd_{10}$, let alone their forbidding crystal structures with 12, 1124, 52 and 28 atomic sites per unit cell.

The Hume-Rothery rules and the Jones model tell us a lot about the factors controlling their stability. For example, for the γ-brass structure, $Cu_5Cd_8$, the Hume-Rothery rules tell us that it should be found at 21/13 $e^-/a$, which it does, and Jones theory tells us that this electron count is controlled by the {3 3 0} and {4 1 1} and other reflections, a result confirmed by pseudo-gap measurements,[92,99–101] high quality band structures,[87,102–105] and even Hückel and extended Hückel theory.[28,94,105] These models certainly tell us a lot about why γ-brass exists. But even with these results, can we see the γ-brass structure as something simple, in the same way that we can think of the structure of one water molecule as simple?

We can't. But perhaps there is a hint that some day we will. All diffraction patterns of all crystals discussed in this paper are all projections of the same 4D Platonic solid. This 4D solid, like all 3D Platonic solids, is in some sense simple. Our Platonic view though is in reciprocal space, not real space. Today, to project the real space structure of γ-brass from an object with just a few sites in its asymmetric unit, we need to project from the 6D $D_6$ or 8D $E_8$ Bravais lattices. (Of these two, the 8D Bravais lattice can capture the full 600-cell point group symmetry while the $D_6$ can not; the point group of $D_6$ being $6!\times 2^5$ element, it cannot be a supergroup of the 600-cell point group, $H_4$, with $5!^2$ group elements.[106]) Perhaps real space geometrical constructions remain to be found, simpler than the known 6D or 8D Bravais projections, whose higher dimensional geometry is solely based on 4D Platonic solids, or their point groups. If so, they would bring us one step closer to thinking of this one class of metal structures as simple and transparent.

## Appendices

**Synthesis and characterization of $Zn_{11}Au_{15}Cd_{23}$**: Samples of $Au_{32}Cd_{47}Zn_{21}$ were prepared by mixing a one gram sample of Au (shaved metal), Cd (powder), and Zn(powder) with nominal 99.9% metal purity and sealing the mixture in an evacuated silica tube. The mixture was heated from room temperature to 650°C over 5 h, held at that temperature for another 5 h, and then cooled to 250°C gradually over a two-week period, after which the furnace was turned off. Microprobe measurements of crystals extracted from the bulk sample yielded a composition of $Zn_{11.0(1)}Au_{15.0(1)}Cd_{23.2(1)}$.

A crystal was then selected for single crystal refinement. Initial refinement with 100% occupation of all sites led to a crystal similar to the one reported, but where the Cd4 site had a thermal factor substantially larger than that of the other sites. We therefore allowed mixed occupation of this site permitting Au, Cd, and Zn to occupy this position, now renamed site M4, while constraining that overall site M4 remained fully occupied. With the inclusion of only these two new parameters $wR_2$ for all reflections lowered from 12.80 to 12.24%, a statistically significant decrease. The final refined crystal stoichiometry (see Table 12) was $Zn_{11.0}Au_{15.0}Cd_{23.0}$, in good agreement with the microprobe measurements, see above.

The refinement procedure used to obtain the M4 site occupancies was as follows: beginning with the M4 site fully occupied by Cd, two new parameters were introduced allowing for Au and Zn occupation at this site, but where the sum of occupation was set at full occupancy. Initially M4 thermal parameters were kept at the isotropic and fixed values of the original Cd4 refinement (Tables 13 and 14). A large damping factor was initially included in the refinement but this damping factor was slowly withdrawn. After the site occupation had reached a stable value, site occupancies were fixed and M4 thermal parameters were released.

These values could be compared with values derived from the microprobe analysis. Microprobe analyses for the crystal as a whole gave $Zn_{11.0(1)}Au_{15.0(1)}Cd_{23.2(1)}$. If we assume that all metal sites are fully occupied and that only the M4 site has mixed metal occupation, these microprobe results lead to M4 Au/Cd/Zn occupation values of 0.27–0.29/0.37–0.39/

Table 12. Crystallographic information and $R$ values for $Zn_{11}Au_{15}Cd_{23}$.

| Empirical formula | $Zn_{11.0}Au_{15.0}Cd_{23.0}$ |
|---|---|
| formula weight | 12958.50 |
| $T$ | 293(2) K |
| $\lambda$ | 0.71073 Å |
| crystal system | cubic |
| space group | $Im\bar{3}$ |
| unit cell dimensions | $a=13.8432(19)$ Å |
| $V$ | 2652.8(6) Å$^3$ |
| $Z$ | 3.2244 |
| $\rho_{calcd}$ | 8.111 Mg m$^{-3}$ |
| $\mu$ | 57.845 mm$^{-1}$ |
| $F(000)$ | 5414 |
| $2\theta$ range for data collection | 2.94 to 37.56° |
| index ranges | $-23 \le h \le 12$<br>$-5 \le k \le 23$<br>$-21 \le l \le 10$ |
| reflections collected | 5781 |
| independent reflections | 1282 [$R_{int}=0.0761$] |
| completeness | 99.6 % |
| absorption correction | semi-empirical from equivalents |
| refinement method | full-matrix least-squares on $F^2$ |
| data/restraints/parameters | 1282/0/38 |
| goodness-of-fit on $F^2$ | 0.775 |
| final $R$ indices [$I>2\sigma(I)$] | $R_1=0.0353$, $wR_2=0.1048$ |
| $R$ indices (all data) | $R_1=0.0533$, $wR_2=0.1224$ |
| largest diff. peak and hole | 2.950 and −4.013 e Å$^{-3}$ |

Table 13. Atomic coordinates ($\times 10^4$) and equivalent isotropic displacement parameters (Å$^2\times 10^3$) for $Zn_{11}Au_{15}Cd_{23}$.

| Site | Occ. | $x$ | $y$ | $z$ | $U_{eq}$[a] |
|---|---|---|---|---|---|
| Au1 | | 0 | 0 | 0 | 18(1) |
| Au2 | | 3306(1) | 0 | 2096(1) | 9(1) |
| Au3 | | 5000 | 0 | 3290(1) | 8(1) |
| M4[b] | 0.27/0.37/0.36 | 1740(1) | 0 | 1027(1) | 29(1) |
| Cd7 | | 5000 | −1178(1) | 5000 | 9(1) |
| Cd8 | | 3031(1) | 1815(1) | 1134(1) | 12(1) |
| Zn9 | | 3331(1) | 0 | 4035(1) | 9(1) |

[a] $U_{eq}$ is defined as one third of the trace of the orthogonalized $U_{ij}$ tensor. [b] The occupation shown for site M4 is the fraction Au/Cd/Zn. Refining the M4 site as a mixture (shown here) rather than pure Cd lowers the $R_1$ value from 3.71 to 3.53 % (for $I>2\sigma(I)$).

0.35–0.38. These values are sufficiently similar to the values obtained independently by refinement (values of 0.27/0.37/0.36) that no further occupation refinement was sought.

**600-Cell to 3D cluster projections**: The 4D to 3D projection matrices used to generate the vertex-, edge-, polygon-, and cell- centered clusters are given in the Supporting Information. The 600-cell 3D projections, which are the result of these projection matrices, are illustrated in Figure 43. As discussed in the text, only the hemisphere of the 600-cell closest to the chosen center of the projection is kept, a procedure analogous to that typically used in orthographic projections of the Earth where only a single hemisphere centered around either the North or South Pole is shown. In our 4D to 3D 600-cell projections, the roles of the North and South Poles have been taken up by the four 600-cell high symmetry positions: the vertex-, the edge-, polygon-, and cell-centers.

A second further constraint is required for metal crystals. Tetrahedra which are almost perfectly regular near the orthographic projection center become entirely flat at the projection equator. Such flattened tetrahedra are implausible as actual metal crystal building blocks. In Figure 43, we have therefore removed all projected vertices which lie at the projection equator itself. In the case of the edge- and polygon-centered projection, vertices, whose projected radius are only 0.9 and 1.3 %, respectively, less than the equatorial radius, have been eliminated as well.

Table 14. Anisotropic displacement parameters (Å$^2\times 10^3$) for $Zn_{11}Au_{15}Cd_{23}$. The anisotropic displacement factor exponent takes the form: $-2\pi^2[h^2a^{*2}U_{11}+\ldots+2hka^*b^*U_{12}]$.

| Site | $U_{11}$ | $U_{22}$ | $U_{33}$ | $U_{23}$ | $U_{13}$ | $U_{12}$ |
|---|---|---|---|---|---|---|
| Au1 | 18(1) | 18(1) | 18(1) | 0 | 0 | 0 |
| Au2 | 9(1) | 9(1) | 8(1) | 0 | 1(1) | 0 |
| Au3 | 7(1) | 12(1) | 6(1) | 0 | 0 | 0 |
| M4 | 20(1) | 29(1) | 38(1) | 0 | −19(1) | 0 |
| Cd7 | 8(1) | 11(1) | 9(1) | 0 | 0 | 0 |
| Cd8 | 14(1) | 10(1) | 12(1) | 2(1) | 0(1) | 2(1) |
| Zn9 | 7(1) | 11(1) | 8(1) | 0 | 2(1) | 0 |

The full hemispheric orthographic projections are shown to the right of Figure 43, while hemispheric orthographic projection with equatorial

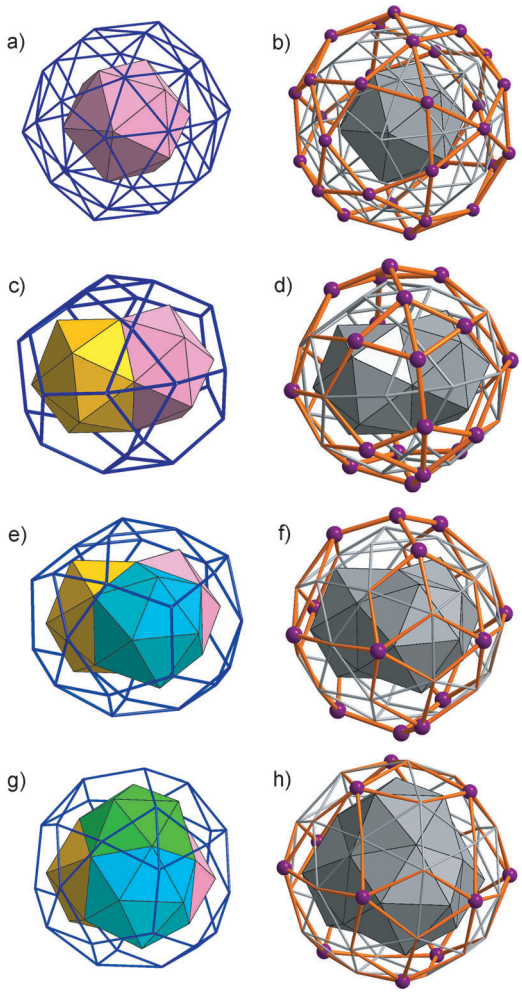


Figure 43. Orthographic hemispheric a), b) vertex-, c), d) edge-, e), f) polygon-, and g), h) cell-centered 3D projections of the 4D 600-cell. Following standard cartographic projections, only the hemisphere closest to the projection center is kept. The left column shows the orthographic projections discussed in the paper text while the right column gives these same projections with the unphysical equatorial and near-equatorial sites included as well.

sites removed are given on the left. The number of vertices removed are 30, 22, 14, and 12 for the vertex-, edge-, polygon-, and cell-centered projections, respectively. These latter projections correspond to the projections used in the main body of this paper.

## Acknowledgements

The authors would like to thank Roald Hoffmann, Neil Ashcroft, and Louis Hand for their patient listening and helpful comments as this work progressed.

[1] F. C. Frank, J. S. Kasper, *Acta Crystallogr.* **1958**, *11*, 184–190.
[2] W. B. Pearson, *The Crystal Chemistry and Physics of Metals and Alloys*, Wiley Series on the Science and Technology of Materials, Wiley-Interscience, New York, **1972**.
[3] M. D. Sikirić, O. Delgado-Friedrichs, M. Deza, *Acta Crystallogr. Sect. A* **2010**, *66*, 602–615.
[4] O. Delgado-Friedrichs, M. O'Keeffe, *Acta Crystallogr. Sect. A* **2010**, *66*, 637–639.
[5] F. C. Frank, J. S. Kasper, *Acta Crystallogr.* **1959**, *12*, 483–499.
[6] Y. P. Yarmolyuk, P. I. Kripyakevich, *Kristallografiya* **1974**, *19*, 539–545.
[7] Y. P. Yarmolyuk, P. I. Kripyakevich, *Sov. Phys. Crystallogr.* **1974**, *19*, 334–337.
[8] D. P. Shoemaker, C. B. Shoemaker, *Acta Crystallogr. Sect. B* **1986**, *42*, 3–11.
[9] F. Laves, H. Witte, *Metallwirtschaft, Metallwissenschaft, Metalltechnik* **1935**, *14*, 645–649.
[10] S. Amerioun, T. Yokosawa, S. Lidin, U. Haussermann, *Inorg. Chem.* **2004**, *43*, 4751–4760.
[11] G. Bergman, J. L. T. Waugh, L. Pauling, *Acta Crystallogr.* **1957**, *10*, 254–259.
[12] S. Samson, *Acta Crystallogr.* **1967**, *23*, 586–600.
[13] S. Andersson, *Acta Crystallogr. Sect. B* **1980**, *36*, 2513.
[14] G. Kreiner, M. Schapers, *J. Alloys Compd.* **1997**, *259*, 83–114.
[15] J. Schmidt, S. Lee, D. C. Fredrickson, M. Conrad, J. Sun, B. Harbrecht, *Chem. Eur. J.* **2007**, *13*, 1394–1410.
[16] M. Feuerbacher, C. Thomas, J. P. A. Makongo, S. Hoffmann, W. Carrillo-Cabrera, R. Cardoso, Y. Grin, G. Kreiner, J.-M. Joubert, T. Schenk, J. Gastaldi, H. Nguyen-Thi, N. Mangelinck-Noel, B. Billia, P. Donnadieu, A. Czyrska-Filemonowicz, A. Zielinska-Lipiec, B. Dubiel, T. Weber, P. Schaub, G. Krauss, V. Gramlich, J. Christensen, S. Lidin, D. Fredrickson, M. Mihalkovic, W. Sikora, J. Malinowski, Janusz, S. Bruehne, T. Proffen, W. Assmus, M. de Boissieu, F. Bley, J.-L. Chemin, J. Schreuer, W. Steurer, *Z. Kristallogr.* **2007**, *222*, 259–288.
[17] O. Gourdon, Z. Izaola, L. Elcoro, V. Petricek, G. J. Miller, *Inorg. Chem.* **2009**, *48*, 9715–9722.
[18] T. Weber, J. Dshemuchadse, M. Kobas, M. Conrad, B. Harbrecht, W. Steurer, *Acta Crystallogr. Sect. B* **2009**, *65*, 308–317.
[19] M. Conrad, B. Harbrecht, T. Weber, D. Y. Jung, W. Steurer, *Acta Crystallogr. Sect. A Acta Crystallogr. Sect. B* **2009**, *65*, 318–325.
[20] J. Dshemuchadse, D. Y. Jung, W. Steurer, *Acta Crystallogr. Sect. B* **2011**, *67*, 269–292.
[21] J. F. Sadoc, R. Mosseri, *Geometrical Frustration*, Cambridge University Press, NewYork, **2006**.
[22] R. F. Berger, S. Lee, J. Johnson, B. Nebgen, F. Sha, J. Q. Xu, *Chem. Eur. J.* **2008**, *14*, 3908–3930.
[23] H. Jones, *Proc. R. Soc. London Ser. A* **1934**, *144*, 225–234.
[24] N. F. Mott, H. Jones, The Theory of the Properties of Metals and Alloys; Clarendon Press: Oxford, **1936**.
[25] V. F. Degtyareva, H. S. Smirnova, *Z. Kristallogr.* **2007**, *222*, 718–721.
[26] R. J. Hoffmann, *J. Am. Chem. Soc.* **1963**, *85*, 1397–1412.
[27] R. Hoffmann, *Solids and Surfaces: A Chemists View of Bonding in Extended Structures*, VCH, New York, **1988**.
[28] R. F. Berger, P. L. Walters, S. Lee, R. Hoffmann, *Chem. Rev.* **2011**, *111*, 4522–4545.
[29] P. Kriyakevich, E. Gladyshevskii, E. Cherkashin, *Doklady Akademii Nauk SSSR* **1952**, *80*, 253–256.
[30] M. Sulonen, *Acta Polytechnica Scandinavica Chemical-metallurgic series* **1962**, *18*, 22.
[31] J. K. Brandon, R. Y. Brizard, P. C. Chieh, R. K. McMillan, W. B. Pearson, *Acta Crystallogr. Sect. B* **1974**, *30*, 1412–1417.
[32] A. J. Bradley, C. H. Gregory, *Philos. Mag.* **1931**, *12*, 143–162.
[33] T. Rajasekharan, K. Schubert, *Z. Metallkunde* **1982**, *73*, 262–264.
[34] D. Shechtman, I. Blech, D. Gratias, J. W. Cahn, *Phys. Rev. Lett.* **1984**, *53*, 1951–1953.
[35] C. S. Lee, G. J. Miller, *J. Am. Chem. Soc.* **2000**, *122*, 4937–4947.
[36] Q. S. Lin, J. D. Corbett, *Inorg. Chem.* **2004**, *43*, 1912–1919.
[37] W. Steurer, *Z. Kristallogr.* **2004**, *219*, 391–446.
[38] C. P. Gomez, S. Lidin, *Chem. Eur. J.* **2004**, *10*, 3279–3285.
[39] M. Duneau, A. Katz, *Phys. Rev. Lett.* **1985**, *54*, 2688–2691.
[40] V. Elser, C. L. Henley, *Phys. Rev. Lett.* **1985**, *55*, 2883–2886.
[41] M. Boudard, M. de Boissieu, C. Janot, G. Heger, C. Beeli, H. U. Nissen, H. Vincent, R. Ibberson, M. Audier, J. M. Dubois, *J. Phys. Condens. Matter* **1992**, *4*, 10149–10168.
[42] S. Lidin, D. Fredrickson, *Symmetry* **2012**, *4*, 537–544.
[43] V. Elser, N. J. A. Sloane, *J. Phys. A* **1987**, *20*, 6161–6167.
[44] J. F. Sadoc, R. Mosseri, *J. Phys. A* **1993**, *26*, 1789–1809.
[45] V. S. Kraposhin, A. L. Talis, J. M. Dubois, *J. Phys. Condens. Matter* **2002**, *14*, 8987–8996.
[46] V. S. Kraposhin, *Met. Sci. Heat Treatment* **2005**, *47*, 351–358.
[47] R. F. Berger, S. Lee, J. Johnson, B. Nebgen, A. C. Y. So, *Chem. Eur. J.* **2008**, *14*, 6627–6639.
[48] R. Mosseri, J. F. Sadoc, *J. Physique* **1986**, *47*, 281–297.
[49] R. Mosseri, J. F. Sadoc, *J. Physique* **1990**, *51*, C7257–C7264.
[50] M. Kleman, J. Friedel, *Rev. Mod. Phys.* **2008**, *80*, 61–115.
[51] N. Rivier, *J. Physique* **1982**, *43*, 91–95.
[52] D. R. Nelson, *Phys. Rev. Lett.* **1983**, *50*, 982–985.
[53] V. Y. Shevchenko, *Search in Chemistry, Biology and Physics of the Nanostate*, Lema, Saint-Petersburg, **2011**.
[54] H. Coxeter, *Regular Polytopes*, Dover Publications, New York, **1973**.
[55] A. J. Bradley, J. Thewlis, *Proc. R. Soc. London Ser. A* **1926**, *112*, 678–692.
[56] A. Westgren, G. Phragmén, *Philos. Mag.* **1925**, 311–341.
[57] A. Johansson, S. Westman, *Acta Chemica Scandinavica* **1970**, *24*, 3471–3479.
[58] S. Thimmaiah, K. W. Richter, S. Lee, B. Harbrecht, *Solid State Sci.* **2003**, *5*, 1309–1317.
[59] N. C. Shi, X. Z. Li, Z. S. Ma, K. H. Kuo, *Acta Crystallogr. Sect. B* **1994**, *50*, 22–30
[60] J. Erassme, H. Lueken, *Acta Crystallogr. Sect. B* **1987**, *43*, 244–250.
[61] Cerius$^2$, Version 4.9, Accelrys, San Diego, **2005**.
[62] S. Samson, *Acta Chem. Scandinavica* **1949**, *3*, 835–843.
[63] S. Kaskel, J. D. Corbett, *Inorg. Chem.* **2000**, *39*, 3086–3091.
[64] J. B. Friauf, *Phys. Rev.* **1927**, *29*, 0034–0040.
[65] A. Bradley, C. Cheng, *Z. Kristallogr.* **1938**, *99*, 480–487.
[66] U. Burkhardt, M. Ellner, Y. Grin, B. Baumgartner, *Powder Diffr.* **1998**, *13*, 159–162.
[67] J. B. J. Friauf, *J. Am. Chem. Soc.* **1927**, *49*, 3107–3114.
[68] J. K. Brandon, R. Y. Brizard, P. C. Chieh, R. K. Mcmillan, W. B. Pearson, *Acta Crystallogr. Sect. B* **1974**, *30*, 1412–1417.
[69] B. J. Beaudry, A. H. Daane, *Trans. Am. Inst. Min. Metall. Pet. Eng.* **1960**, *218*, 854–859.
[70] K. Nassau, L. V. Cherry, W. E. Wallace, *J. Phys. Chem. Solids* **1960**, *16*, 123–130.
[71] A. E. Dwight, *J. Less-Common Met.* **1975**, *43*, 117–120.
[72] A. E. Dwight, *Trans. Am. Soc. Met.* **1961**, *53*, 479–500.
[73] K. Sugiyama, N. Kaji, K. Hiraga, T. Ishimasa, *Z. Kristallogr.* **1998**, *213*, 90–95.
[74] Y. Matsuo, K. Hiraga, *Philos. Mag. Lett.* **1994**, *70*, 155–161.

  

[75] C. B. Shoemaker, D. A. Keszler, D. P. Shoemaker, *Acta Crystallogr. Sect. B* **1989**, *45*, 13–20.
[76] G. Kreiner, H. F. Franzen, *J. Alloys Compounds* **1997**, *261*, 83–104.
[77] W. Steurer, *Philos. Mag.* **2006**, *86*, 1105–1113.
[78] W. Steurer, S. Deloudi, *Acta Crystallogr. Sect. A* **2008**, *64*, 1–11.
[79] R. Berger, S. Lee, R. Hoffmann, *Chem. Eur. J.* **2007**, *13*, 7852–7863.
[80] V. Y. Shevchenko, V. A. Blatov, G. D. Ilyushin, *Glass Phys. Chem.* **2009**, *35*, 1–12.
[81] V. Y. Shevchenko, V. A. Blatov, G. D. Ilyushin, *Struct. Chem.* **2009**, *20*, 975–982.
[82] V. A. Blatov, G. D. Ilyushin, D. M. Proserpio, *Inorg. Chem.* **2011**, *50*, 5714–5724.
[83] W. Hume-Rothery, *The Metallic State*, Clarendon Press, Oxford, **1931**.
[84] W. Hume-Rothery, *Electrons, Atoms, Metals, and Alloys*, Dover, New York, **1963**.
[85] A. T. Paxton, M. Methfessel, D. G. Pettifor, *Proc. R. Soc. London Ser. A* **1997**, *453*, 1493–1514.
[86] G. T. de Laissardière, D. Nguyen-Manh, D. Mayou, *Progress in Materials Science* **2005**, *50*, 679–788.
[87] U. Mizutani, *Hume-Rothery Rules for Structurally Complex Alloy Phases*, CRC Press, Boca Raton, **2011**.
[88] A. P. Sutton, M. W. Finnis, D. G. Pettifor, Y. Ohta, *J. Phys. C* **1988**, *21*, 35–66.
[89] T. E. Stacey, D. C. Fredrickson, *Dalton Trans.* **2012**, *41*, 7801–7813.
[90] N. W. Ashcroft, N. D. Mermin, *Solid state physics*, Holt, New York, **1976**.
[91] H. Sato, R. S. Toth, G. Honjo, *J. Phys. Chem. Solids* **1967**, *28*, 137–160.
[92] T. B. Massalski, U. Mizutani, *Progr. Mater. Sci.* **1978**, *22*, 151–262.
[93] H. Sato, R. S. Toth, *Phys. Rev. Lett.* **1962**, *8*, 239–241.
[94] L. M. Hoistad, S. Lee, *J. Am. Chem. Soc.* **1991**, *113*, 8216–8220.
[95] A. L. Mackay, *Acta Crystallogr.* **1962**, *15*, 916.
[96] T. Takeuchi, U. Mizutani, *Phys. Rev. B* **1995**, *52*, 9300–9309.
[97] U. Mizutani, R. Asahi, H. Sato, T. Noritake, T. Takeuchi, *J. Phys. Condens. Matter* **2008**, *20*, 275–228.
[98] T. B. Massalski, H. Okamoto, *Binary alloy phase diagrams*, 2nd ed., ASM International, Materials Park, Ohio, **1990**.
[99] U. Mizutani, A. Kamiya, T. Matsuda, K. Kishi, S. Takeuchi, *J. Phys. Condens. Matter* **1991**, *3*, 3711–3718.
[100] S. J. Poon, *Adv. Phys.* **1992**, *41*, 303–363.
[101] Q. S. Lin, J. D. Corbett, *J. Am. Chem. Soc.* **2007**, *129*, 6789–6797.
[102] T. Takeuchi, H. Sato, U. Mizutani, *J. Alloys Compd.* **2002**, *342*, 355–359.
[103] U. Mizutani, T. Takeuchi, H. Sato, *Progr. Mater. Sci.* **2004**, *49*, 227–261.
[104] R. Asahi, H. Sato, T. Takeuchi, U. Mizutani, *Phys. Rev. B* **2005**, *71*, 165103.
[105] O. Gourdon, D. Gout, D. J. Williams, T. Proffen, S. Hobbs, G. J. Miller, *Inorg. Chem.* **2007**, *46*, 251–260.
[106] R. V. Moody, J. Patera, *J. Phys. A* **1993**, *26*, 2829–2853.

Received: October 20, 2012
Revised: March 15, 2013
Published online: ■■ ■■, 0000

  

Intermetallic Phases

*S. Lee,* R. Henderson, C. Kaminsky, Z. Nelson, J. Nguyen, N. F. Settje, J. T. Schmidt, J. Feng* ..... ■■■■–■■■■

**Pseudo-Fivefold Diffraction Symmetries in Tetrahedral Packing**

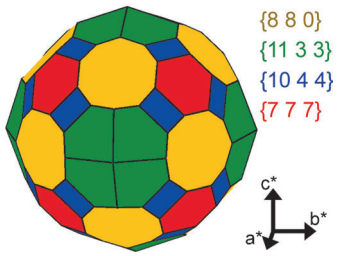


**Hidden symmetries**: Metal crystal structures such as $Cd_3Cu_4$ (see figure) with its 1124 atom unit cell continue to intrigue. Why do such simple stoichiometries form such complex forms? Fivefold pseudosymmetries prove to be a unifying theme. In newly prepared $Zn_{11}Au_{15}Cd_{23}$, the pseudosymmetries lead to an electron count which, to three significant figures, accords with experiment.